Volume 35 | Issues 1–2 | 2014
Included in this print edition:
Issue 1 (January 5, 2014)
Issue 2 (January 15, 2014)

Journal of COMPUTATIONAL CHEMISTRY

Organic • Inorganic • Physical
Biological • Materials

www.c-chem.org

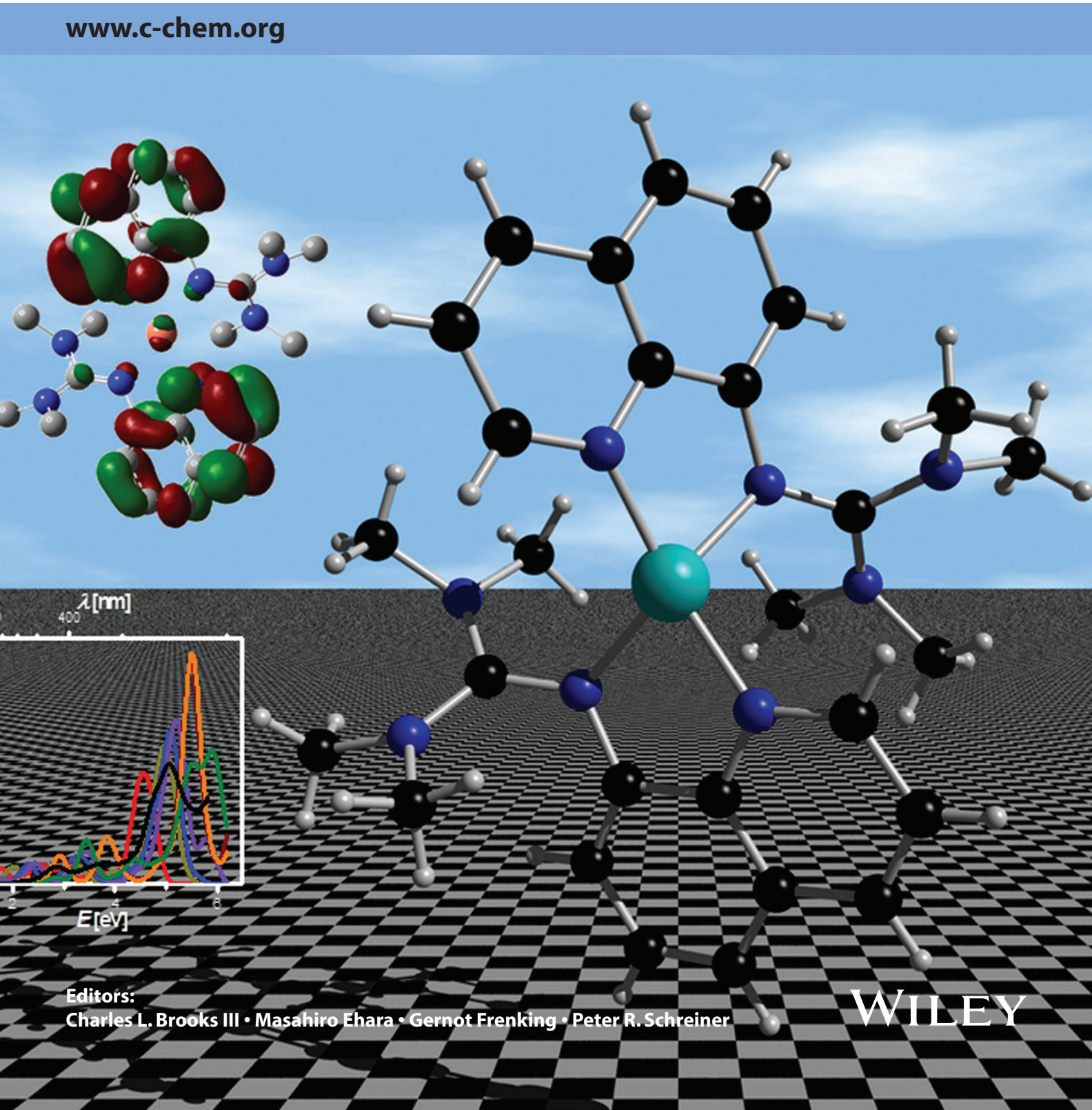

WILEY

Journal of COMPUTATIONAL CHEMISTRY
Organic • Inorganic • Physical
Biological • Materials

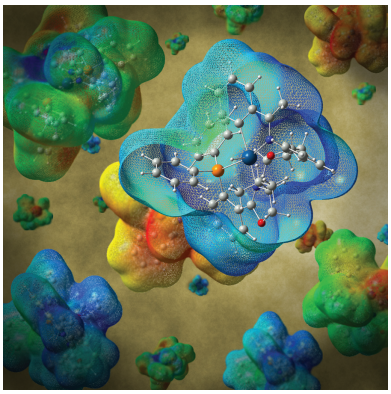

Organometallic Complexes

An extension of the VALBOND-trans force field for iridium complexes is introduced by Franziska Hofmann, Michael Devereux, Andreas Pfaltz, and Markus Meuwly on page 18. Newly fitted, transferable parameters capture the structure and interactions of a chemically diverse set of ligands, depicted on the cover using the electrostatic potential of interacting species mapped onto their isodensity surfaces. A recently developed, "supervised" fitting approach is used to obtain the parameters, combining the efficiency of computational fitting with the crucial extra stability that human supervision can provide for highly correlated and nonlinear fitting problems.

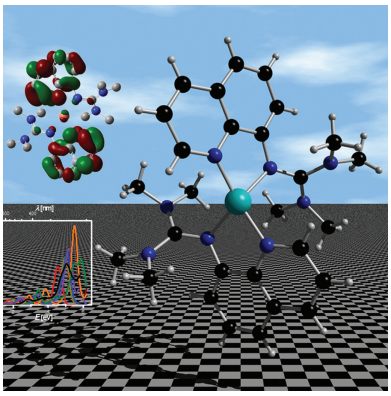

Many-Body Perturbation Theory

A comprehensive study on the structural and optical properties of a guanidine–quinoline copper(I) bis(chelate) complex is reported by Sonja Herres-Pawlis et al. on page 1. This complex displays interesting metal–ligand charge-transfer behavior. In order to probe the applicability of time-dependent density functional theory (TDDFT) to charge-transfer excitations in these complexes, many-body perturbation theory calculations are performed for a small model system. The TDDFT optical response agrees at least qualitatively with the spectrum obtained from the Bethe–Salpeter equation based on quasiparticle energies within the GW approximation. However, the TDDFT results strongly depend on the exchange and correlation functional, and need careful benchmarking.

Coming Soon

Look for these important papers in upcoming issues

Assessing protein–ligand docking for the binding of organometallic compounds to proteins

Elisabeth Ortega-Carrasco et al.

Organometallic compounds are increasingly used as molecular scaffolds in drug development projects. In this study, the predictiveness of protein–ligand docking programs for the binding of inert organometallic scaffolds with protein receptors is investigated. Using the software GOLD as an illustrative case, scoring functions, preprocessing calculations, and flexibility schemes are tested.
DOI: 10.1002/jcc.23472

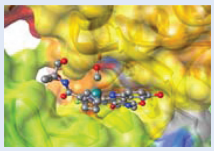

Highly asymmetric electrolytes in the primitive model: Hypernetted chain solution in arbitrary spatial dimensions

Marco Heinen et al.

A numerically robust and efficient Fourier–Bessel transform technique is applied to solve liquid integral equations for ion pair correlations in electrolytes in an arbitrary number of spatial dimensions. The method is applicable in very large ranges of ion size- and charge-asymmetries, including values that correspond to micrometer-sized charged colloidal particles in electrolytes of subnanometer-sized, monovalent microions.
DOI: 10.1002/jcc.23446

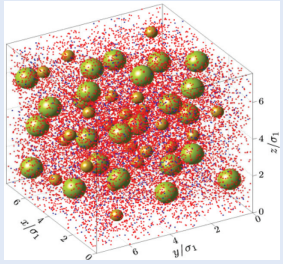

Geometrical and Optical Benchmarking of Copper Guanidine–Quinoline Complexes: Insights from TD-DFT and Many-Body Perturbation Theory†

Anton Jesser,[a] Martin Rohrmüller,[b] Wolf Gero Schmidt,[b] and Sonja Herres-Pawlis*[a]

We report a comprehensive computational benchmarking of the structural and optical properties of a bis(chelate) copper(I) guanidine–quinoline complex. Using various (TD-)DFT flavors a strong influence of the basis set is found. Moreover, the amount of exact exchange shifts metal-to-ligand bands by 1 eV through the absorption spectrum. The BP86/6-311G(d) and B3LYP/def2-TZVP functional/basis set combinations were found to yield results in best agreement with the experimental data. In order to probe the general applicability of TD-DFT to excitations of copper bis(chelate) charge-transfer (CT) systems, we studied a small model system that on the one hand is accessible to methods of many-body perturbation theory (MBPT) but still contains simple guanidine and imine groups. These calculations show that large quasiparticle energies of the order of several electronvolts are largely offset by exciton binding energies for optical excitations and that TD-DFT excitation energies deviate from MBPT results by at most 0.5 eV, further corroborating the reliability of our TD-DFT results. The latter result in a multitude of MLCT bands ranging from the visible region at 3.4 eV into the UV at 5.5 eV for the bis(chelate) complex. Molecular orbital analysis provided insight into the CT within these systems but gave mixed transitions. A meaningful transition assignment is possible, however, by using natural transition orbitals. Additionally, we performed a thorough conformational analysis as the correct description of the copper coordination is crucial for the prediction of optical spectra. We found that DFT identifies the correct conformational minimum and that the MLCTs are strongly dependent on the torsion of the chelate angles at the copper center. From the results, it is concluded that extensive benchmarking allows for the quantitative analyses of the CT behavior of copper bis(chelate) complexes within TD-DFT. © 2013 Wiley Periodicals, Inc.

DOI: 10.1002/jcc.23449

Introduction

Copper is an extremely important transition metal for catalysts, biological molecules such as proteins, and building blocks for molecular magnets.[1–6] With its rich coordination chemistry, copper containing systems have been extensively studied both experimentally and theoretically. These copper complexes are mainly stabilized by nitrogen donor ligands ensuring high relevance to metalloproteins and their models.[7,8] By variation of kind and strength of donor as well as of ligand denticity and geometric restrictions, the chemical properties of the copper complexes can be tailored to the desired application in coordination chemistry, catalysis or bioinorganic chemistry.[2,7–9]

Guanidines convince by their good donor properties for numerous transition metals and their strong nucleophilicity.[10–12] Especially in the coordination of copper, guanidines have proven to be useful for the activation of dioxygen[13,14] or atom transfer radical polymerization.[15,16] In our recent studies, we investigate copper bis(chelate) complexes as charge-transfer (CT) systems. In this study, we focus on the geometry, the electronic structure and optical absorption spectra of a cationic Cu(I) complex with an aromatic hybrid guanidine ligand using density-functional theory (DFT) and time-dependent (TD-) DFT methods. DFT is computationally efficient and applicable to many problems, but the functional sensitivity causes problems for TD-DFT, especially for CT systems.[17]

Here we report on extensive DFT calculations on a guanidine–quinoline copper(I) bis(chelate) complex. This complex possesses highly interesting charge transfer properties and a great importance as electron transfer system (Hoffmann et al., manuscript in preparation).[18] We highlight the importance of the amount of exact exchange in the functional as well as of the basis set for theoretical predictions of structure and optical spectra. In many studies, rather small basis sets such as LANL2DZ have been used for the description of the copper atom.[19,20] We apply Pople and Ahlrichs basis sets of double or triple zeta quality with different amounts of diffusion and polarization functions. As benchmarks, we use experimental structure data from single crystal X-ray analysis[18] and UV/Vis

[a] A. Jesser, S. Herres-Pawlis
Ludwig-Maximilians-Universität München, Department Chemie, Butenandtstr. 5-13, 81377 München, Germany
E-mail: sonja.herres-pawlis@cup.uni-muenchen.de
[b] M. Rohrmüller, W. G. Schmidt
Universität Paderborn, Department Physik Lehrstuhl für Theoretische Physik, Warburger Str. 100, 33095 Paderborn, Germany

†Dedicated to Prof. Dr. Willi Kantlehner on the occasion of his 70th birthday.

Contract/grant sponsor: Deutsche Forschungsgemeinschaft; Contract/grant number: FOR 1405; Contract/grant sponsor: Fonds der Chemischen Industrie; Contract/grant sponsor: Bundesministerium für Bildung und Forschung; Contract/grant number: MoSGrid initiative 01IG09006

absorption spectra. It is worth noting that bis(chelate) complexes with unsymmetrical bidentate ligands yield chiral complexes. Special attention has been paid to conformational analysis and isomer analysis of the investigated copper(I) complex. Extensive conformational analyses for copper(I) diimine complexes with ligands of the phenathroline family have been performed by other groups, focussing on the influence of the coordination geometry on the metal-to-ligand-charge-transfer (MLCT) behavior.[21,22]

The optical excitations of the guanidine–quinoline copper(I) bis(chelate) complex are calculated here within the linear-response approach to TD-DFT. While presently TD-DFT is the method of choice to address charge neutral excitations in complex molecules, the approach has to be considered with some caution. It is well founded in principle, but the actual numerical implementations rely on the adiabatic approximation and are plagued with the well-known shortcomings of the electron exchange and correlation (XC) functionals used in the DFT calculations. In particular, the application of TD-DFT to states that have CT character may be problematic and can cause errors of the order of electronvolts (for details see, e.g., Ref. [23]). For this reason, we use a complementary approach, namely many-body perturbation theory (MBPT)[24] to assess the applicability and reliability of TD-DFT for the class of molecules to be studied here. The MBPT or Green's function approach is at least in principle not plagued by the shortcomings of the XC functionals used within DFT. It starts from the screening response of the electronic system after electronic or optical excitation. Here the excitation energies correspond to the poles of single- and two-particle Green's functions. From the one-electron Green's function, single-particle excitations such as ionization energies or electron affinities are obtained and the two-particle Green's function allows to access electron-hole pair energies and plasmons. In practice, the optical response is obtained from the solution of the Bethe-Salpeter equation (BSE), see, for example, Ref. [24]. Unfortunately, the latter class of calculations is computationally far more demanding than TD-DFT and can only be performed for relatively small systems. For this reason, we benchmark the TD-DFT results to MBPT for a model system, namely $[CuN_8C_8H_{16}]^+$, a smaller nonsubstituted imine-guanidine bis(chelate) copper(I) complex which is expected to show excitations that are comparable in nature to those of the more complicated guanidine–quinoline copper(I) bis(chelate) complex.

Theoretical Methods

The geometries of the complex cations $[Cu(TMGqu)_2]^+$ and $[CuN_8C_8H_{16}]^+$ (named as small system) are fully optimized at different levels of DFT using the Berny algorithm as implemented in Gaussian 09.[25] All optimized geometries are characterized as stationary points on the potential energy surface (PES) with vibrational frequency calculations. TD-DFT calculations are performed on the equilibrium ground state geometries with different DFT levels.

The Gaussian 09 calculations are performed with the local generalized-gradient approximations (GGA) BP86,[26,27] BLYP,[27–29] and PW91,[30–32] the nonlocal hybrid GGAs B3LYP,[27,28,33,34] BHLYP[27,28] and PBE0,[35] the local meta GGA TPSS,[36] the nonlocal hybrid meta GGA TPSSh,[36] the long-range corrected wB97XD[37] functional including empirical dispersion and the hybrid Coulomb-attenuating CAM-B3LYP[38] functional. Pople[39–46] and Ahlrichs[47] type basis sets 6–31G(d), 6–31+G(d), 6-311G(d), 6-311+G(d), 6-311G(2d,2p), def2-SVP, and def2-TZVP are used. Continuous spectra are plotted with the SWizard program[48,49] using the Gaussian model. The half-bandwidths were taken to be equal to 3000.0 cm^{-1}.

In addition to the localized basis sets, we also perform calculations using a plane-wave basis. Plane waves form, by construction, a complete and orthogonal basis set. Its numerical convergence can be smoothly varied and reliably controlled. The plane-wave calculations in this work start from the molecular electronic structure obtained from the Vienna *ab initio* simulation package[50] implementation of DFT. Core ions are described by projector augmented-wave pseudopotentials.[51] A cubic supercell with a lattice constant of 16 Å, implicating periodic boundary conditions, is used wherein the minimum distance between atoms of periodic replica molecules is 7.5 Å. Complete numerical convergence is found for a plane-wave cutoff energy of 380 eV. This value is used throughout. The electron XC functional used for structure optimization has only a minor effect on the optical properties as will be shown below. Therefore we focus on the PW91 GGA functional for this purpose.

In addition to TD-DFT, optical spectra are calculated on different levels of MBPT. The independent-particle approximation (IPA)[52–55] is the simplest approach in this respect. It allows for a simple and often intuitive interpretation of the optical spectra in terms of transitions between the single-particle states obtained within DFT. A more realistic description of the optical excitation is achieved by solving the BSE. It can be written as a two-particle Schrödinger equation of electrons (v) and holes (c). The resonant part of the exciton Hamiltonian,[56] that is, the Hamiltonian in Tamm-Dancoff approximation (TDA) is given by

$$H_{v,v',c,c'} = (\varepsilon_c - \varepsilon_v)\delta_{vv'}\delta_{cc'} + 2\int\int dr dr' \Psi_c^*(r)\Psi_v(r)\bar{v}(r-r')\Psi_{c'}(r')\Psi_{v'}^*(r') - 2\int\int dr dr' \Psi_c^*(r)\Psi_{c'}(r)W(r,r')\Psi_v(r')\Psi_{v'}^*(r').$$

The diagonal term is determined by the quasiparticle transition energies. They are determined here within the GW approximation (GWA) to the Hedin equations,[57,58] using the implementation described in Ref. [59]. Thereby an energy cutoff of 100 eV and 128 frequency points are used. The second part of the Hamiltonian describes the electron-hole exchange via the short-range part of the bare Coulomb potential $\bar{v}$, reflecting the influence of local fields. The last term corresponds to the screened electron-hole attraction, calculated here using the model dielectric function proposed in Ref. [60]. This approach was originally developed for inorganic semiconductors, but has meanwhile been successfully applied to a variety of molecular systems.[61–64] As the TDA has been

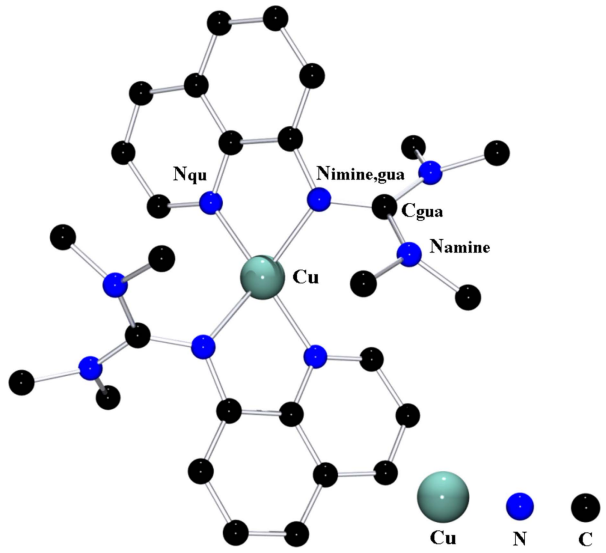

Figure 1. Structure of $[Cu(TMGqu)_2]^+$ cation in solid state (experimental data following single crystal X-ray diffraction analysis). [Color figure can be viewed in the online issue, which is available at wileyonlinelibrary.com.]

shown to break down for a series of molecular systems,[65–68] we also present results that were obtained by including additionally the antiresonant and resonant–nonresonant coupling terms in the electron-hole Hamiltonian. The actual solution of the BSE is done by either a direct diagonalization or by using the time-evolution approach developed by one of the present authors.[69] Thereby all electron-hole pairs within an energy window of 20 eV are taken into account. The static dielectric constant entering the model dielectric function is determined in an iterative scheme as described in Ref. [64]. We estimate the numerical approximations entering the actual calculations of quasiparticle energies within the GWA and the exciton binding energies within the BSE to result in an error bar of 0.2 eV for the peak positions.

Results and Discussion

Structural benchmarking

As the prediction of structures is always the first step in computational chemistry, all following steps depend considerably on its accuracy. Thus, great attention should be paid to an adequate description of the molecule's chemical bonding situation and its electronic structure. To assess the accuracy of the various theoretical methods used here, the comparison with an experimentally obtained structure such as from X-ray crystallography is very helpful. In the case of the $[Cu(TMGqu)_2]^+$ cation (Fig. 1), several crystal structures with the counter anions PF_6^-, ClO_4^-, and OTf^- exist (Hoffmann et al., manuscript in preparation).[18] All but one contain one complex cation with C_1 symmetry in the asymmetrical unit, whereas the complex with PF_6^- crystallises with 1.5 cationic species in the asymmetrical unit, the 0.5 deriving from a species with C_2 symmetry. The structures show only small differences, the highest deviations being in the Cu—N bond lengths. The coordination motif is a distorted tetrahedron with an angle between the CuN_2 planes in the range of 64.7–68.3°, with 90° being a perfect tetrahedron. The τ_4-value can also be used to describe the coordination.[70] In addition to the first coordination sphere, attention is paid to the description of the guanidine moiety, specifically the C—N bonds of the central CN_3 group and the structural parameter ρ.[71] For calculation of ρ, the formula $\rho = 2a/(b+c)$ applies, where a is the C=N bond length and b and c are the C—NR_2 bond lengths. In case of a total delocalization of the double bond within the guanidine moiety, ρ is equal to one. Selected structural parameters are summarized in Table 1. For comparative reasons average values of each parameter are provided.

The quality of description at a given level of DFT can be evaluated by calculating the deviation of a theoretically obtained value from its experimental counterpart by using $(p_{i,calc} - p_{i,exp})/p_{i,exp}$*100.

It should be noted that in comparison of crystal structure data to gas-phase optimized DFT results the matrix effect of the solid state is neglected. Moreover, the confidence interval σ has to be multiplied by three to cover 98% uncertainty. When applying this 3 σ interval, the agreement of the calculations is high.

With the hybrid GGA B3LYP and the two pure GGAs BLYP and BP86 extensive benchmarking calculations are performed. Therefore, geometries with the basis sets 6-31G(d), 6-31+G(d), 6-311G(d), def2-SVP, and def2-TZVP are optimized at each level of theory and compared to selected experimental structural parameters. The results are summarized in Table 2.

The Cu—N bond lengths are underestimated with 6-31G(d), with values between −3.3 and −0.8%. Addition of diffuse

Table 1. Selected bond lengths (Å), angles (°) and structural parameters of $[Cu(TMGqu)_2]^+$ cation in solid state with different anions. (Hoffmann et al., Manuscript in preparation).[18]

Anion	PF_6^- (C_1)	PF_6^- (C_2)	ClO_4^-	OTf^-	average
Cu—$N_{imine,gua}$ (Å)	2.095(3), 2.068(3)	2.077(3)	2.080(3), 2.074(3)	2.065(2), 2.113(3)	2.081
Cu—N_{qu} (Å)	1.966(3), 1.999(3)	1.999(3)	2.002(3), 1.998(3)	2.003(2), 1.978(3)	1.993
C=$N_{imine,gua}$ (Å)	1.330(4), 1.316(4)	1.323(4)	1.312(4), 1.319(4)	1.324(4), 1.321(4)	1.321
C—N_{amine} (Å)	1.355(5), 1.363(5)	1.356(5), 1.362(5)	1.359(4), 1.361(4)	1.356(4), 1.359(4)	1.360
	1.357(5), 1.365(5)		1.352(4), 1.362(4)	1.356(4), 1.372(4)	
ρ	0.98, 0.97	0.97	0.96, 0.97	0.98, 0.97	0.97
∠(CuN_2—CuN_2) (°)	65.1	64.7	68.3	68.0	66.5
τ_4	0.58	0.57	0.61	0.61	0.59

The experimental uncertainty is given in form of the confidence interval σ written in parentheses after the values of the bond lengths and angles.

Table 2. Calculated structural parameters and deviations of $[Cu(TMGqu)_2]^+$ cation.

Level of theory	Cu—$N_{imine,gua}$ (Å)		Cu—N_{qu} (Å)		C=$N_{imine,gua}$ (Å)		C—N_{amine} (Å)			∠ (CuN_2—CuN_2) (°)	ρ	τ_4
B3LYP/6-31G(d)	2.049	−1.5%	1.977	−0.8%	1.327	0.5%	1.368	1.377	0.9%	73.0	0.97	0.66
B3LYP/6-31+G(d)	2.160	3.8%	2.045	2.6%	1.327	0.5%	1.368	1.377	0.9%	78.6	0.97	0.69
B3LYP/def2-SVP	2.146	3.1%	2.064	3.6%	1.324	0.2%	1.367	1.377	0.9%	74.7	0.97	0.66
B3LYP/6-311G(d)	2.091	0.5%	2.059	3.3%	1.321	0.0%	1.365	1.376	0.8%	68.0	0.96	0.60
B3LYP/def2-TZVP	2.174	4.5%	2.052	3.0%	1.320	−0.1%	1.362	1.371	0.5%	77.8	0.97	0.68
BLYP/6-31G(d)	2.047	−1.6%	1.962	−1.6%	1.344	1.7%	1.380	1.389	1.8%	73.4	0.97	0.67
BLYP/6-31+G(d)	2.173	4.4%	2.017	1.2%	1.343	1.7%	1.380	1.391	1.9%	78.4	0.97	0.69
BLYP/def2-SVP	2.148	3.2%	2.041	2.4%	1.340	1.4%	1.379	1.389	1.8%	75.4	0.97	0.67
BLYP/6-311G(d)	2.123	2.0%	1.997	0.2%	1.338	1.3%	1.378	1.389	1.7%	68.1	0.97	0.61
BLYP/def2-TZVP	2.186	5.0%	2.023	1.5%	1.337	1.2%	1.374	1.384	1.4%	77.6	0.97	0.68
BP86/6-31G(d)	2.012	−3.3%	1.942	−2.6%	1.342	1.6%	1.374	1.383	1.4%	70.6	0.97	0.65
BP86/6-31+G(d)	2.107	1.2%	1.996	0.3%	1.342	1.6%	1.374	1.384	1.4%	77.2	0.97	0.69
BP86/def2-SVP	2.104	1.1%	2.019	1.3%	1.338	1.3%	1.374	1.383	1.4%	73.5	0.97	0.65
BP86/6-311G(d)	2.060	−1.0%	1.986	−0.4%	1.336	1.1%	1.372	1.382	1.2%	66.3	0.97	0.60
BP86/def2-TZVP	2.123	2.0%	2.000	0.4%	1.335	1.1%	1.368	1.378	1.0%	76.9	0.97	0.68

functions to 6-31+G(d) yields larger Cu—N values but also leads to overestimation at B3LYP and BLYP levels with values between 1.2 and 4.4%, and good agreement for BP86 (0.3 and 1.2%). Similar tendency is found for def2-SVP. The triple-zeta basis set 6-311G(d) yields larger Cu—N bond lengths than 6-31G(d), with most values between −1.0 and 2.0% showing small deviations from experimental data, and the biggest error for the Cu—N_{qu} bond at B3LYP level with 3.3%. Def2-TZVP yields the largest overestimation of the Cu—N bond lengths, with values between 0.4 and 5.0%. Compared to the other two functionals, the Cu—N bond lengths at the BP86 level of theory are smaller for each basis set. Because of this, good agreement with experimental data is achieved for each basis set except 6-31G(d), with values between −1.0 and 2.0%.

The C—N bond lengths of the guanidine moiety show almost no dependency on the basis set, with errors decreasing from 6-31G(d) to def2-TZVP at each level of theory. Here, best results are obtained with B3LYP, with deviations of −0.1 to 0.5% for the double bond and 0.5 to 0.9% for the single bond. The other two functionals yield errors between 1.0 and 1.9%, with BP86 performing slightly better. At each level of theory, smallest deviations are obtained with def2-TZVP. The proportions of double to single bonds and thus the degree of delocalization of the guanidine moiety described by the structural parameter ρ are predicted correctly at each level of theory.

Remarkably, the angle between the CuN_2 planes is overestimated for up to 12° with each basis set except of 6-311G(d). But as the degree of distortion of the first coordination sphere has to be quite sensitive to the matrix effect in the solid state, deviations from the dihedral angles in the gas-phase optimized structures are to be expected.

To inspect the influence of the functional on the prediction of structural parameters the performances of several density functionals in combination with the def2-TZVP basis set are compared. The results are summarized in Table 3.

As shown in comparison with the other basis sets, def2-TZVP yields an accurate representation of the C—N bonds of the guanidine moiety for each functional used, ranging from −1.3 to 1.2% for the double bond and from −0.4 to 1.4% for the single bonds. The Cu—N bonds are overestimated to varying extent, the largest deviations of about 5% shown by the BLYP GGA and the B3LYP and BHLYP hybrid functionals. Good overall performance is achieved by the PW91 and the BP86 GGAs, the TPSS meta GGA and the TPSSh hybrid meta GGA, with deviations from 0.2 to 2.0%. The PBE0 hybrid functional and the long-range corrected wB97XD functional perform rather well with deviations ranging from 1.9 to 2.3%. It should be mentioned that the wB97XD functional corrects in a

Table 3. Calculated structural parameters and deviations of $[Cu(TMGqu)_2]^+$ cation for various functionals at def2-TZVP basis set.

Level of theory	Cu—$N_{imine,gua}$ (Å)		Cu—N_{qu} (Å)		C=$N_{imine,gua}$ (Å)		C—N_{amine} (Å)			∠ (CuN_2—CuN_2) (°)	τ_4
PW91	2.112	1.5%	1.996	0.2%	1.332	0.8%	1.366	1.374	0.7%	74.6	0.66
BP86	2.123	2.0%	2.000	0.4%	1.335	1.1%	1.368	1.378	1.0%	76.9	0.68
BLYP	2.186	5.0%	2.023	1.5%	1.337	1.2%	1.374	1.384	1.4%	77.6	0.68
TPSS	2.105	1.2%	1.999	0.3%	1.333	0.9%	1.365	1.375	0.7%	75.6	0.67
B3LYP	2.174	4.5%	2.052	3.0%	1.320	−0.1%	1.362	1.371	0.5%	77.8	0.68
PBE0	2.122	2.0%	2.037	2.2%	1.316	−0.4%	1.355	1.363	−0.1%	75.5	0.66
BHLYP	2.165	4.0%	2.106	5.7%	1.304	−1.3%	1.351	1.359	−0.4%	78.6	0.68
TPSSh	2.111	1.4%	2.014	1.1%	1.326	0.4%	1.361	1.37	0.4%	75.9	0.67
wB97XD	2.121	1.9%	2.038	2.3%	1.311	−0.8%	1.358	1.363	0.0%	74.1	0.64
CAM-B3LYP	2.139	2.8%	2.052	3.0%	1.312	−0.7%	1.356	1.365	0.0%	77.0	0.67

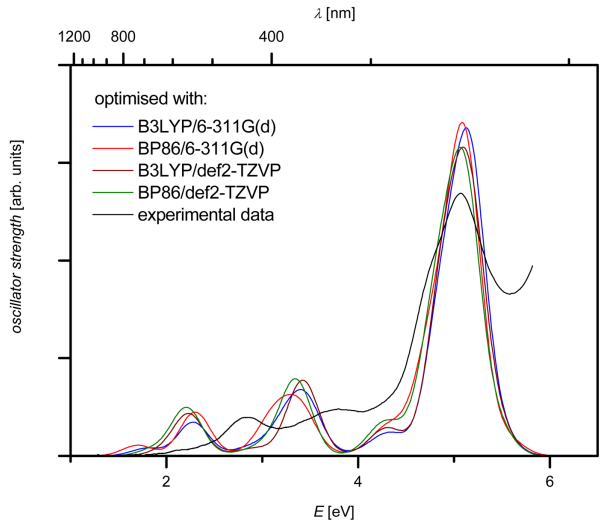

Figure 2. Optical absorption spectra of $[Cu(TMGqu)_2]^+$ calculated within TD-DFT at B3LYP/6-311G(d) for various start geometries obtained from the structural relaxation using the XC functional indicated.

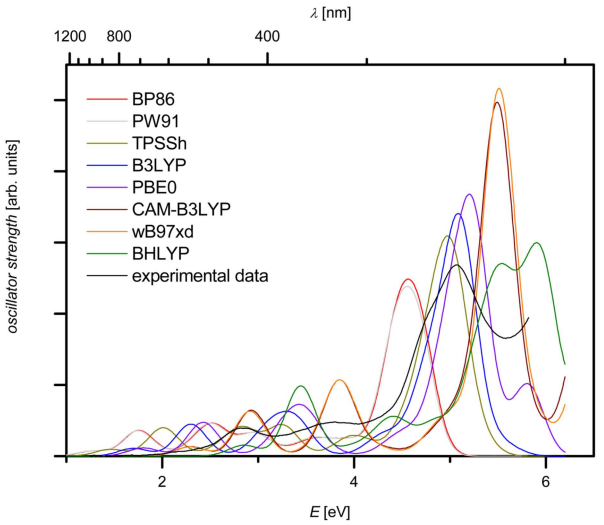

Figure 4. Calculated absorption spectra of $[Cu(TMGqu)_2]^+$ with the 6-311G(d) basis set and various functionals. [Color figure can be viewed in the online issue, which is available at wileyonlinelibrary.com.]

semiempirical manner[72] for the dispersion interaction missing in local XC functionals. Our results do not indicate, however, a significant influence of van der Waals forces on the structural properties of $[Cu(TMGqu)_2]^+$. The Coulomb-attenuating CAM-B3LYP yields rather high errors of about 3%. In summary, the gas-phase calculation at BP86/6-311G(d) level yields the best structural description of the solid state reference data.

Optical benchmarking

Based on the geometrical benchmarking the optical response of the $[Cu(TMGqu)_2]^+$ cation is investigated. Optical absorption spectra are calculated using the linear-response approach to TD-DFT as implemented in Gaussian 09 and compared to experimental data.

The performance of various pure and hybrid XC functionals and basis sets is surveyed. Furthermore, the influence of the start geometry on calculated spectra is shown. The experimental absorption spectrum of the $[Cu(TMGqu)_2]^+$ cation is dominated by three absorption bands (Figs. 2–5): Two bands of MLCT nature at 2.84 and 3.80 eV with molar absorption coefficients $\varepsilon < 10{,}000\ M^{-1}\ cm^{-1}$, and one π-π^* absorption band at 5.07 eV with $\varepsilon = 53{,}700\ M^{-1}\ cm^{-1}$. Additionally, a low-intensity shoulder is observed at ~2.15 eV.

From the geometrical benchmarking, several optimized structures have been obtained which differ in bond lengths and angles in varying extent, and from which some are predicted with different degree of distortion of the first coordination sphere. To assess the influence of the start geometry on TD-DFT results, the calculated spectra of four geometries optimized with the pure BP86 and the hybrid B3LYP functional and the triple zeta basis sets 6-311G(d) and def2-TZVP are compared. Therefore, TD-DFT at B3LYP/6-311G(d) theory level is performed on these geometries. The HOMO–LUMO gap

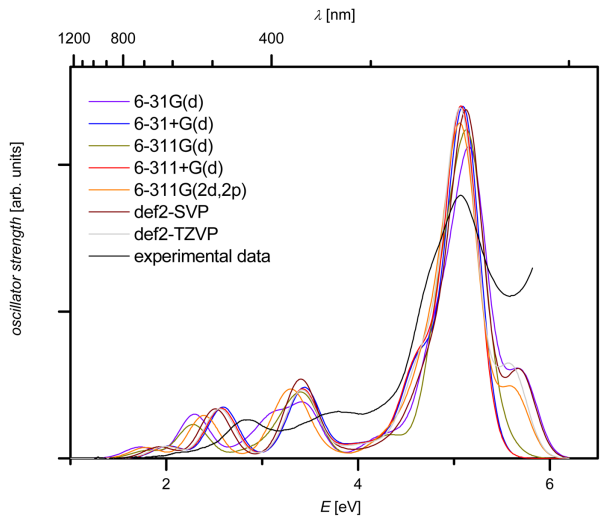

Figure 3. Calculated absorption spectra of $[Cu(TMGqu)_2]^+$ at B3LYP level for various basis sets.

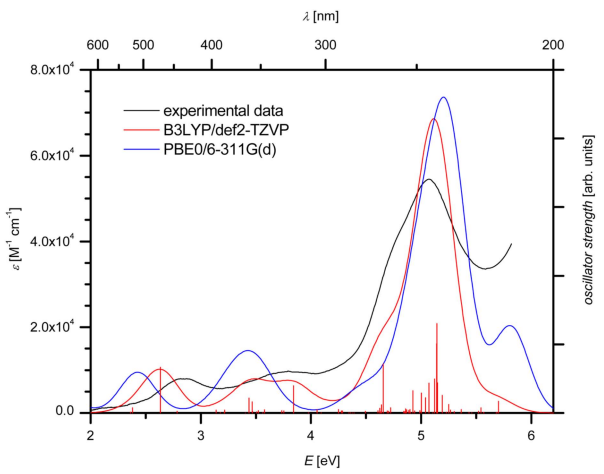

Figure 5. Experimental (black) and calculated (B3LYP/def2-TZVP, red; PBE0/6-311G(d), blue) absorption spectra of $[Cu(TMGqu)_2]^+$. [Color figure can be viewed in the online issue, which is available at wileyonlinelibrary.com.]

Table 4. Calculated HOMO–LUMO gaps and positions of absorption bands at various theory levels.

Start geometry	TD-DFT	E_g (eV)	E_1 (eV)	E_2 (eV)	E_3 (eV)
Experimental		2.15	2.84	3.80	5.07
B3LYP/6-311G(d)	B3LYP/6-311G(d)	1.77	2.28	3.40	5.13
BP86/6-311G(d)	B3LYP/6-311G(d)	1.68	2.31	3.29	5.08
B3LYP/def2-TZVP	B3LYP/6-311G(d)	1.95	2.23	3.42	5.10
BP86/def2-TZVP	B3LYP/6-311G(d)	1.86	2.21	3.34	5.07
Functional	basis set	E_g (eV)	E_1 (eV)	E_2 (eV)	E_3 (eV)
B3LYP	6-31G(d)	1.70	2.29	3.14, 3.42	5.16
	6-31+G(d)	1.99	2.60	3.44	5.09
	6-311G(d)	1.68	2.28	3.40	5.13
	6-311+G(d)	1.97	2.57	3.42	5.07
	6-311G(2d,2p)	1.76	2.39	3.30	5.06
	def2-SVP	1.90	2.51	3.40	5.13
	def2-TZVP	1.96	2.56	3.42	5.06
BP86	6-311G(d)	1.23	1.76	2.52, 2.95	4.56
PW91		1.22	1.75	2.50, 2.94	4.55
TPSSh		1.43	2.01	2.84, 3.24	4.98
B3LYP		1.68	2.29	3.29	5.09
PBE0		1.79	2.43	3.43	5.20
CAM-B3LYP		2.27	2.93	3.85	5.49
BHLYP		2.82	3.44	4.40	5.53, 5.91

energy E_g (S_1 transition) and the positions of the absorption maxima E_1 to E_3 are summarized in the first part of Table 4. The spectra are shown in Figure 2.

The differences in structural parameters result in high deviations in the HOMO–LUMO gap energy E_g and the position of the first band E_1. The 6-311G(d) optimized structures with the larger distortion (vide supra) show smaller E_g and slightly higher E_1 than structures optimized with def2-TZVP but both values deviate by 0.2–0.6 eV from experiment. The larger distance between the first excited state and the first absorption band (which is composed mainly of the S_3 transition) leads to a resolution of the shoulder at ~1.7 eV (S_1 transition) from the main band, which is not observed in the experiment, being a hint on a possibly smaller degree of distortion in solution compared to solid state.

For the second and third absorption band, the influence of the degree of distortion seems to vanish. The geometries optimized with B3LYP show slightly higher E_2 than those with def2-TZVP, the differences in E_3 are negligible. Overall, the positions of the first two bands are underestimated by ~0.5 eV whereas the highest deviation in E_g amounts to 0.27 eV. The position of the third band is quite accurately predicted.

Various double and triple zeta basis sets are used at B3LYP level of TD-DFT on a given start geometry to assess the basis set influence on calculated spectra. The obtained spectra are shown in Figure 3 and the HOMO–LUMO gap energies E_g as well as the positions of the absorption maxima E_1 to E_3 are summarized in the second part of Table 4.

The positions of the second and third absorption bands show little dependence on the basis set save for 6-31G(d) which exhibits a splitting of the second band. There are, however, higher deviations in E_g with values ranging from 1.68 to 1.99 eV and E_1 with values from 2.28 to 2.60 eV. The energies of all bands but the third one are underestimated, and the use of the larger triple zeta basis sets shows no improvement to the double zeta basis sets. Additional polarization functions in 6-311G(2d,2p) shift the first two bands to higher energies and the 6-31+G(d) and 6-311+G(d) basis sets with diffuse functions perform even better. The Ahlrichs basis sets def2-SVP and def2-TZVP yield similar results as the Pople basis sets with added diffuse functions.

At last, to assess the influence of the density functional, spectra with various pure and hybrid GGAs are calculated (Fig. 4). The HOMO–LUMO gap energies E_g and the positions of the absorption maxima are listed in the third part of Table 4. Here, a huge dependence on the functional becomes obvious for the positions of all three absorption bands. The largest underestimation is observed for the pure GGAs BP86 and PW91, the hybrid GGAs TPSSh, B3LYP, and PBE0 lying in between, and the Coulomb-attenuating CAM-B3LYP showing overestimation of all bands' positions. The hybrid functional BHLYP with the highest exact exchange shows the worst performance of all tested functionals, exhibiting the largest overestimation, a low intensity of the second band and a splitting of the third. Additionally, splittings of the second band are observed for BP86, PW91, and TPSSh.

In conclusion, the most important issue in calculating optical absorption spectra of the $[Cu(TMGqu)_2]^+$ cation is the choice of the density functional. The start geometry, and thus the ground-state optimization, as well as the basis set seem to have much less influence on the TD-DFT results. From the results shown above, it becomes clear that the position of the third absorption band is highly dependent on the functional but shows almost no dependence on the start geometry and the basis set. Thus, a functional, which predicts the position of the third band correctly, in combination with a large enough basis set and an appropriate start geometry should prove best suitable for TD-DFT calculations of the $[Cu(TMGqu)_2]^+$ cation

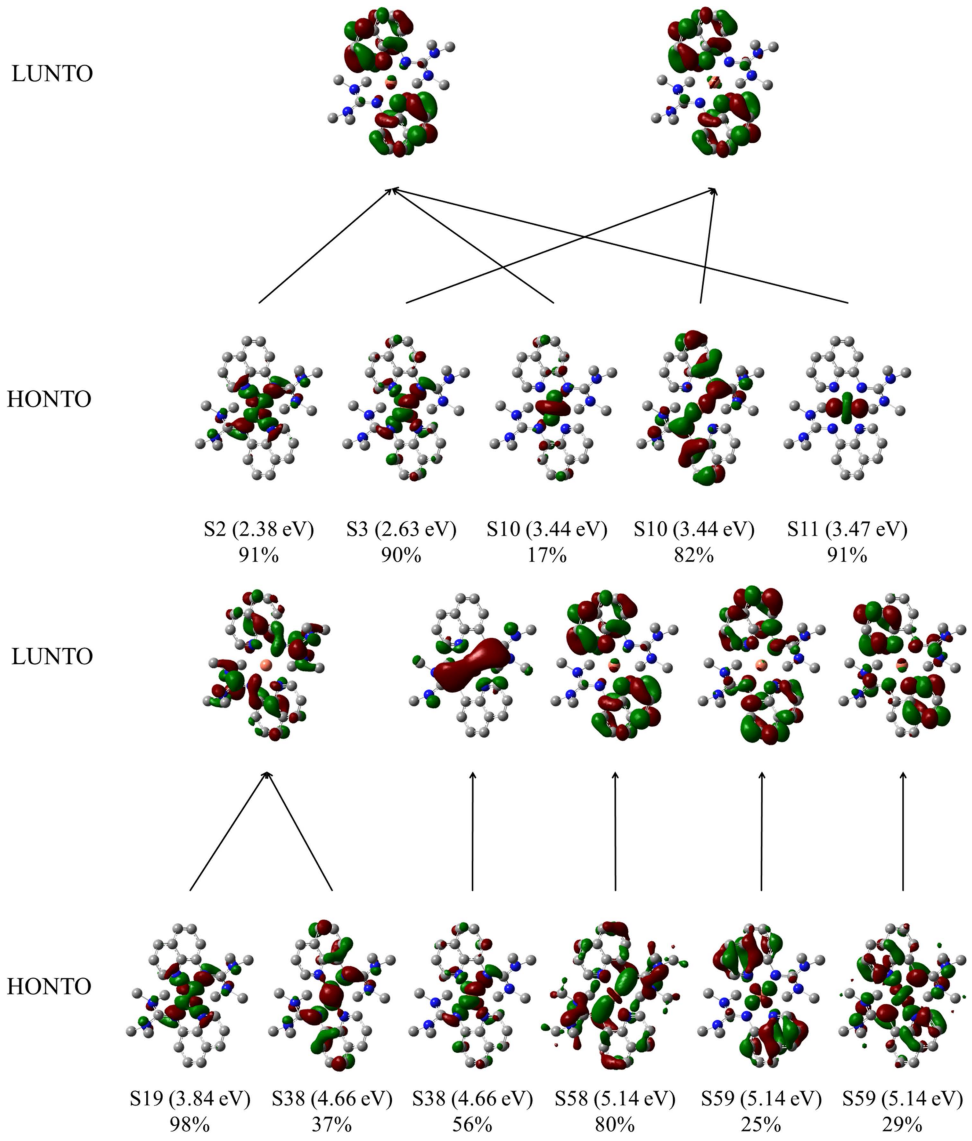

Figure 6. Natural Transition Orbitals (NTOs) for the dominant transitions of $[Cu(TMGqu)_2]^+$ cation at B3LYP/def2-TZVP level of theory. [Color figure can be viewed in the online issue, which is available at wileyonlinelibrary.com.]

and similar compounds. Good accordance to experiment is achieved at B3LYP/def2-TZVP level (Fig. 5), even reproducing the shoulder of the third band at 4.66 eV. The importance of the amount of exact exchange from Hartree-Fock for TD-DFT calculations is also seen in literature, where hybrid GGAs like B3LYP are preferably used.[6,73]

Orbital analysis has shown that the transitions are heavily mixed with regard to the orbitals and their character. Hence, a natural transition orbital (NTO) analysis has been performed[74] based on the TD calculation at B3LYP/def2-TZVP level. The NTO analysis yields an unambiguous donor–acceptor pair for most cases, thus facilitating the assignment of the transition nature. The most prominent transitions in UV and Vis range have been analyzed (Fig. 6). In the Vis range, the excited states S2 (2.38 eV), S3 (2.63 eV), S10 (3.44 eV), and S11 (3.47 eV) stem from MLCT transitions from occupied Cu-d orbitals to empty π*-orbitals of the quinoline parts of the ligands. The acceptor orbitals correspond highly to the LUMO and LUMO+1 molecular orbitals (see below for molecular orbitals discussion). The excited states in the UV range stem from MLCT transitions from occupied Cu-d orbitals to higher-lying π*-orbitals of the ligand with larger guanidine character (S19, 3.84 eV; S38, 4.66 eV) or from MLCT lower-lying occupied mixed orbitals with Cu-d as well as ligand character to LUMO type π*-orbitals of the quinoline (S58, 5.14 eV; S59, 5.14 eV). For most transitions, unambiguous donor–acceptor pairs with a contribution of $>$90% have been found. For S10, a dominant donor–acceptor pair with 82% and a second one with 17% were predicted. Both the acceptor orbitals are different linear combinations of the π*-orbitals of the quinoline whereas both donor orbitals are of Cu-d character, the donor orbital with the higher percentage shows some mixing with quinoline π*-orbitals. For S38, one orbital pair with 56% and another one with 37% have been found. Both transitions are of MLCT type, with Cu-d donor orbitals and higher-lying ligand π* acceptor orbitals. For S59, the assignment is much more ambiguous:

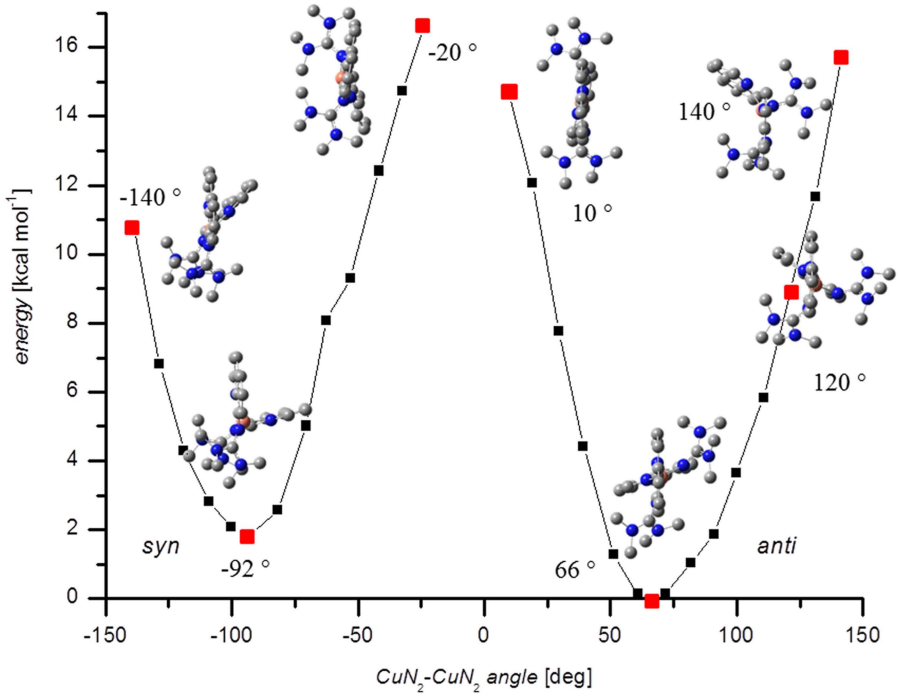

Figure 7. PES curves of $[Cu(TMGqu)_2]^+$ dependent on CuN_2—CuN_2 dihedral angle. [Color figure can be viewed in the online issue, which is available at wileyonlinelibrary.com.]

donor–acceptor pairs with 29 and 25% as well as three other (omitted) with percentages between 10 and 15% have been found. For these, the donor orbitals are still heavily mixed with Cu-d and ligand character. The nature of these transitions cannot be assigned clearly even with help of NTO analysis, but seems to be a mixture of different MLCT and ligand centered π-π^* transitions.

Conformational analysis

Besides XC functionals, reproducing of UV/Vis spectra is highly sensitive to the coordination environment at the copper center.[17] Therefore, we studied the PES of the $[Cu(TMGqu)_2]^+$ cation dependent on the dihedral angle between the CuN_2 coordination planes of the ligands to achieve better understanding of the origin of distortion in the coordination polyhedron.

This investigation is carried out at the BP86/6-311G(d) level of theory. Structural benchmarking results show that at this level, minimal deviations from experimental crystal structure data occur (vide supra). Furthermore, the angle between the chelate planes $\angle(CuN_2—CuN_2)$ is predicted to be 66.3°, which is in accordance with crystal structure data, whereas other basis sets yield larger values. This angle between the chelate planes is highly important for the correct description of the coordination since its value represents the distortion between tetrahedral (90°) and square-planar coordination (0°).

The angle $\angle(CuN_2—CuN_2)$ is changed in steps of ~10° in GaussView. To fix this chelate plane angle, four of the six bond angles in the coordination polyhedron ($N_{imine,gua}$—Cu—N'_{qu}, $N_{imine,gua}$—Cu—$N'_{imine,gua}$, N_{qu}—Cu—$N'_{imine,gua}$, N_{qu}—Cu—N'_{qu}) are frozen with the ModRedundant option of the Opt keyword in Gaussian 09, whereas the bite angles of the ligands are relatively constant and need no fixation. Then, the other parameters are optimized for the given dihedral angle. With this method, a steep parabola with its minimum at 66.3° is obtained (Fig. 7), with energy differences of 14.7 and 15.7 kcal/mol at 9.6 and 141.2°, respectively. Optimizations after further distortion in small steps to both sides in the direction of square planar configuration prove to be unstable because of the guanidine moieties getting too close to each other. Thus, the square planar geometry cannot be assessed due to the sterically demanding hybrid guanidine ligand TMGqu. Rotation beyond the 0/180° limit (square planar) and the following full optimization leads to an unexpected second local minimum, with a dihedral angle of −92.7°, being 1.9 kcal/mol higher in energy than the global minimum at 66.3°. For the second minimum as well, the PES is studied dependent on the dihedral angle, resulting in a similar steep parabola with energy differences of 10.8 and 16.6 kcal/mol at −138.6 and −24.2°.

The structure at the second minimum is identified as a stereoisomer of the $[Cu(TMGqu)_2]^+$ cation, obtained through a hypothetical rotation of the ligands toward each other, which is not possible in experiment. Same result, however, can be achieved via dissociation and reassociation of the kinetically labile Cu complex.

The isomers differ in the orientation of the guanidine moiety in respect to the coordination plane CuN_2. In the free TMGqu ligand, the guanidine moiety is not in-plane with the quinoline rings, but is rotated along the C—N bond which links the guanidine to the quinoline (Scheme 1, left). Thus, in the more

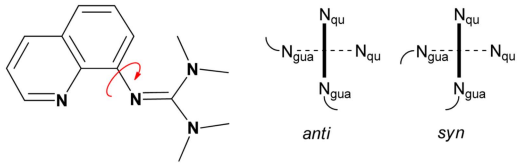

Scheme 1. Alignment of the guanidine moiety due to rotation along C—N bond (left); *anti* and *syn* isomers of a hybrid guanidine bischelate complex (right). [Color figure can be viewed in the online issue, which is available at wileyonlinelibrary.com.]

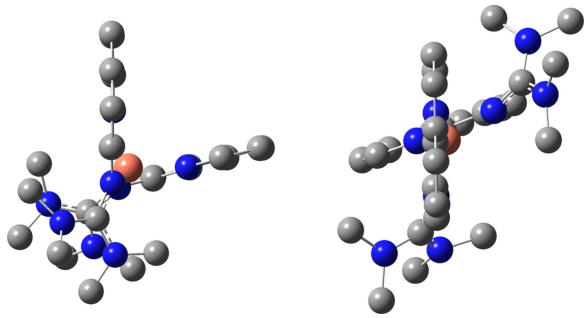

Figure 8. Optimised structures for the *syn* (left) and the *anti* (right) isomers of $[Cu(TMGqu)_2]^+$ at B3LYP/6–311G(d). [Color figure can be viewed in the online issue, which is available at wileyonlinelibrary.com.]

stable isomer found in crystal structures of several copper hybrid guanidine complexes, the guanidine moieties of both ligands are aligned with a maximal distance (Hoffmann et al., manuscript in preparation).[18] This isomer is further called the *anti* isomer. In the second isomer, the *syn* isomer, the guanidine moieties are very close (Scheme 1, right). *Syn* hybrid guanidine complexes with copper have not yet been observed, whereas with zinc both isomers have been crystallized for the $[Zn(TMGmqu)_2][CF_3SO_3]_2$ complex.[75] Optimized structures for both isomers are shown in Figure 8. Relative energies and selected structural parameters are summarized in Table 5.

The variation of the chelate plane angle $\angle(CuN_2—CuN_2)$ is accompanied by significant changes in other structural parameters. A great impact is observed on the Cu—N bonds (Fig. 9). In the minimum at 66.3° (*anti*), the Cu—$N_{imine,gua}$ bond lengths amount to 2.060 Å and thus are longer than the Cu—N_{qu} bonds with 1.986 Å. Between 10 and 66.3° the Cu—$N_{imine,gua}$ bond lengths increase even more and the Cu—N_{qu} bond lengths decrease, until a difference of almost 0.5 Å is attained for 10° (2.402, 1.908 Å).

Between 66.3 and 100° a slight increase of both bond lengths is observed. From 120° on the favored C_2 symmetry of the $[Cu(TMGqu)_2]^+$ cation is lost and the two hybrid guanidine ligands behave differently whereas one ligand exhibits a much longer Cu—$N_{imine,gua}$ bond than the Cu—N_{qu} bond (2.225 vs. 1.956 Å at 140°), with the situation reversed for the other ligand (2.019 vs. 2.133 Å at 140°). This leads to splitting of the plotted curve on the right hand side of Figure 9.

In the minimum at −92.7° (*syn*), the Cu—$N_{imine,gua}$ bonds are slightly longer than the Cu—N_{qu} bonds (2.038 vs. 2.029 Å). Between −140° and −92.7° the Cu—N_{qu} bond lengths increase significantly (2.023 vs. 2.094 Å at −140°). For smaller dihedral angles all Cu—N bond lengths increase slightly, until

Table 5. Relative energies and structure parameters of selected points on the PES of $[Cu(TMGqu)_2]^+$ dependent on the $CuN_2—CuN_2$ angle.

$\angle(CuN_2—CuN_2)$ (°)	ΔE (kcal/mol)	Cu—$N_{imine,gua}$ (Å)	Cu—N_{qu} (Å)	$\angle(CN_3—CuN_2)$ (°)	$\varphi_{N=C}$ (°)	$\varphi_{C—N}$ (°)	ρ
−140	10.8	2.023	2.094	44.0	49.5	13.0	0.971
−130	6.8	2.026	2.065	41.5	44.6	17.3	0.970
−120	4.3	2.031	2.046	39.7	40.9	21.3	0.968
−110	2.8	2.031	2.037	38.5	38.3	25.0	0.969
−100	2.1	2.034	2.032	37.6	36.4	28.2	0.968
−92	**1.9**	**2.038**	**2.029**	**37.7**	**34.8**	**31.0**	**0.968**
−80	2.6	2.044	2.031	39.1	31.4	36.5	0.968
−70	5.0	2.056	2.034	41.3	27.9	43.4	0.967
−60	8.1	2.066	2.043	44.1	25.4	49.1	0.967
−50	9.3	2.112	2.004	74.0	43.0	47.7	0.976
−40	12.4	2.191	1.968	80.0	46.0	46.4	0.973
−30	14.7	2.301	1.930	79.8	46.9	47.1	0.970
−20	16.6	2.397	1.905	80.7	50.3	43.3	0.969
10	14.7	2.402	1.908	60.0	55.1	15.4	0.970
20	12.1	2.239	1.942	57.9	57.5	14.1	0.971
30	7.8	2.159	1.966	51.5	52.5	15.8	0.970
40	4.4	2.104	1.981	48.9	47.8	18.8	0.971
50	1.3	2.075	1.983	45.7	41.4	22.9	0.971
60	0.1	2.062	1.986	44.5	37.5	27.7	0.970
66	**0.0**	**2.060**	**1.986**	**44.3**	**36.1**	**29.9**	**0.970**
70	0.2	2.060	1.986	43.7	34.5	32.3	0.970
80	1.0	2.068	1.984	43.9	32.5	36.2	0.970
90	1.9	2.076	1.981	44.8	31.1	39.3	0.970
100	3.7	2.084	1.982	47.6	29.7	44.5	0.971
110	5.8	2.080	1.997	56.7	30.7	51.0	0.973
120	8.9	2.084	2.012	60.3	29.3	56.7	0.974
130	11.7	2.157, 2.059	1.985, 2.053				
140	15.7	2.225, 2.019	1.956, 2.133				

Bold numbers indicate local minima.

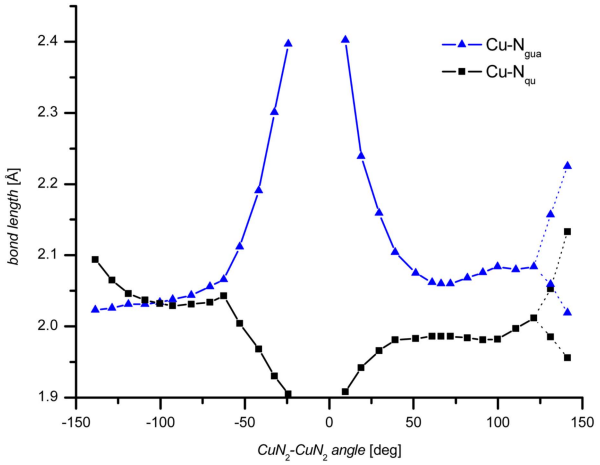

Figure 9. Changes in Cu—N bond lengths dependent on CuN_2—CuN_2 angle. [Color figure can be viewed in the online issue, which is available at wileyonlinelibrary.com.]

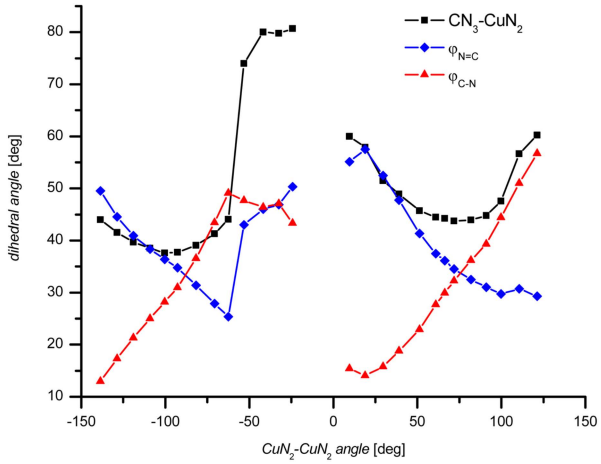

Figure 10. Changes in orientation of the guanidine moiety dependent on CuN_2—CuN_2 angle. [Color figure can be viewed in the online issue, which is available at wileyonlinelibrary.com.]

at −60° a large increase in the Cu—$N_{imine,gua}$ bond lengths and a rapid decrease in the Cu—N_{qu} bond lengths are observed reaching again a difference of almost 0.5 Å (2.397 vs. 1.905 Å at −20°).

Additionally, a large influence on the orientation of the guanidine moiety in respect to the coordination plane CuN_2 of the ligand is observed. The orientation can be described with the angle between the CuN_2 plane and the plane of the CN_3 guanidine moiety, but essentially it is determined by the rotations along the C_{qu}—$N_{imine,gua}$ single bond linking the quinoline to the guanidine, and along the $N_{imine,gua}$=C_{gua} double bond of the guanidine, as shown in Scheme 2. These rotations are expressed with the dihedral angles $\varphi_{C(qu)—N(imine,gua)}$ [(C^1–C^2–N^3–C^4, red) for the C_{qu}—$N_{imine,gua}$ rotation] and $\varphi_{N(imine,gua)=C(gua)}$ [(C^2–N^3–C^4–N^5, blue) for the $N_{imine,gua}$=C_{gua} rotation].

In both minima, the plane angle ∠(CN_3—CuN_2) is smallest (*syn*: 37.7°; *anti*: 44.3°) and increases to both sides of the curves on the PES.

The plot of the dihedral angles $\varphi_{C(qu)—N(imine,gua)}$ and $\varphi_{N(imine,gua)=C(gua)}$ against the angle ∠(CuN_2—CuN_2) yields nearly linear curves for a large part of the investigated range (Fig. 10). The dihedral angle $\varphi_{C(qu)—N(imine,gua)}$ increases and $\varphi_{N(imine,gua)=C(gua)}$ decreases with increasing ∠(CuN_2—CuN_2) in the ranges from −140 to −60° and from 20 to 120°. Between

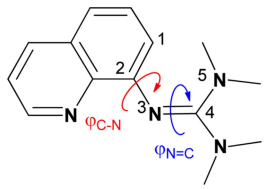

Scheme 2. Orientation of the guanidine moiety relative to the quinoline rings. The rotation around the dihedral angles $\varphi_{C(qu)—N(imine,gua)}$ [(C^1 – C^2 – N^3 – C^4, red) for the C_{qu}—$N_{imine,gua}$ rotation] and $\varphi_{N(imine,gua)=C(gua)}$ [(C^2 – N^3 – C^4 – N^5, blue) for the $N_{imine,gua}$—C_{gua} rotation] are visualized by arrows. [Color figure can be viewed in the online issue, which is available at wileyonlinelibrary.com.]

−60 and 20° a continuous transition between the *syn* and the *anti* isomer is foreshadowed, but cannot be assessed because of the splitting of the ligand situation due to high sterical demands of the guanidine moieties (vide supra and Fig. 9). Results for ∠(CuN_2—CuN_2) larger 120° are neglected because of the loss of the C_2 symmetry.

The dependence of a rotational angle in the guanidine on the angle between the coordination planes ∠(CuN_2—CuN_2) is not intuitively clear at first sight. The rotation along $\varphi_{C(qu)—N(imine,gua)}$ influences the coordination geometry, because the orientation of the coordinating $N_{imine,gua}$ determines the orbital overlapping with the central metal atom. Additionally, the rotation along $\varphi_{N(imine,gua)=C(gua)}$ influences the delocalization of the double bond in the guanidine moiety and thus π interactions of ligand and metal. According to that, the reverse connection between coordination geometry and rotations in the guanidine moiety is possible. As shown above, via the rotation along $\varphi_{C(qu)—N(imine,gua)}$ the isomerisation of *anti* to *syn* or vice versa is possible (compare Scheme 1). Thus, a second investigation of the PES is conducted, in dependence on the dihedral angle $\varphi_{C(qu)—N(imine,gua)}$. For this investigation, only the two dihedral angles have to be fixed with the Mod-Redundant option, starting again from the optimised *anti* minimum with $\varphi_{C(qu)—N(imine,gua)}$ equal to 29.9°. The angles are modified in 10° steps, then fixed and the structures optimized. A dihedral angle $\varphi_{C(qu)—N(imine,gua)}$ of 0° describes a parallel orientation of the guanidine to the quinoline, and thus, to the coordination plane. The change from *anti* to *syn* means a change of $\varphi_{C(qu)—N(imine,gua)}$ from a positive to a negative value, with positive values for the *anti* and negative values for the *syn* isomer.

The dihedral angle $\varphi_{C(qu)—N(imine,gua)}$ of the *anti* isomer is investigated between −30 and 120° and yields a perfect parabola reaching relative energies of 21.4 and 31.4 kcal/mol (Fig. 11). A second minimum for negative $\varphi_{C(qu)—N(imine,gua)}$ values is not observed. Then, the investigation of the PES of the *syn* isomer is conducted, with a similar perfect parabola and maximal relative energies of 30.3 and 28.7 kcal/mol at −110

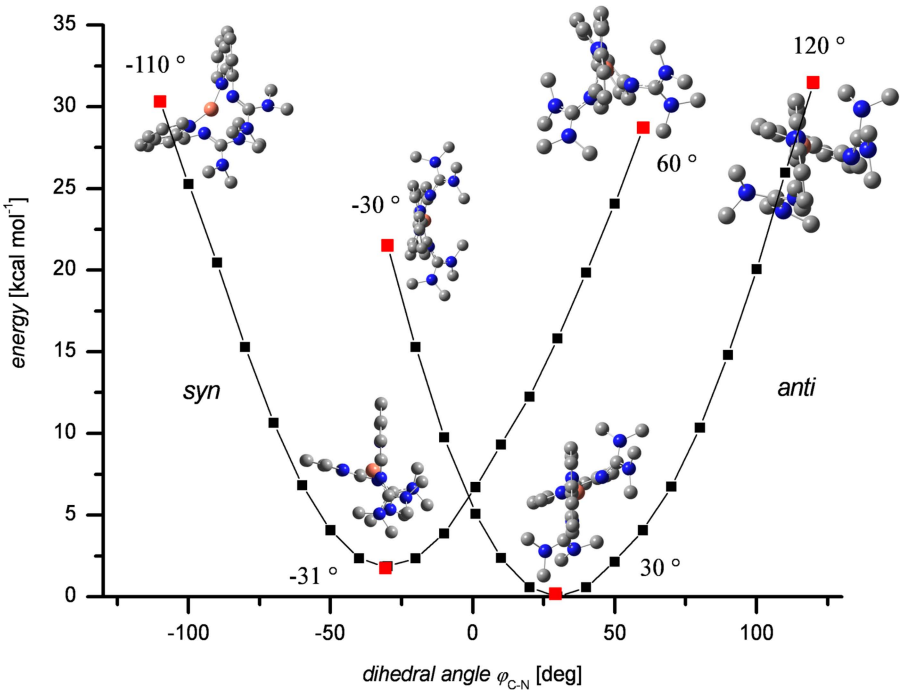

Figure 11. PES curves of $[Cu(TMGqu)_2]^+$ dependent on rotation along the C—$N_{imine,gua}$ single bond. [Color figure can be viewed in the online issue, which is available at wileyonlinelibrary.com.]

and 60° respectively, and the minimum at −31°. Here as well, no second minimum is found; rather the curves show an intersection for ~0° and 6 kcal/mol. Relative energies and selected structural parameters are summarized in Table 6.

The plot of the dihedral angles ∠(CuN_2—CuN_2) from the first PES investigation against $\varphi_{C(qu)—N(imine,gua)}$ for both isomers yields two almost linear curves with equal slopes (Fig. 12).

Why the transition from *anti* to *syn* via rotation of the $\varphi_{C(qu)-N(imine,gua)}$ is not possible, becomes clear from a closer look at the guanidine moieties of both isomers: The NMe_2 groups of the guanidine can also adopt different orientations, as shown in Scheme 3. All structures obtained starting from the *anti* isomer in Figure 11 exhibit the same orientations of the NMe_2 groups, but differ from the orientations in the *syn* isomer. The influence of these orientations has been confirmed by changing them manually in GaussView. A subsequent optimization results in a structure with lower relative energy, and after removal of the ModRedundant fixation, in the minimum of the other isomer.

The change of the orientation of the NMe_2 groups from one isomer to the other involves the rotations along both C_{gua}—N_{amine} bonds in both ligands. These rotations are sterically

Table 6. Relative energies of selected points on the PES of $[Cu(TMGqu)_2]^+$ dependent on the $\varphi_{C—N}$ dihedral angle.

syn			*anti*		
$\varphi_{C—N}$ (°)	Δ*E* (kcal/mol)	∠(CuN_2—CuN_2) (°)	$\varphi_{C—N}$ (°)	Δ*E* (kcal/mol)	∠(CuN_2—CuN_2) (°)
−110	30.3	43.7	−30	21.4	30.7
−100	25.3	46.0	−20	15.3	38.8
−90	20.5	60.9	−10	9.8	44.5
−80	15.3	68.8	0	5.1	50.5
−70	10.6	73.8	10	2.4	55.6
−60	6.8	78.2	20	0.6	60.9
−50	4.1	82.6	**30**	**0.0**	66.3
−40	2.4	87.8	40	0.6	71.9
−31	**1.9**	92.7	50	2.1	77.5
−20	2.4	103.6	60	4.1	89.8
−10	3.9	109.3	70	6.7	95.0
0	6.7	112.4	80	10.4	99.0
10	9.3	114.0	90	14.8	102.9
20	12.3	119.3	100	20.1	105.9
30	15.8	123.0	110	26.0	108.2
40	19.9	124.5	120	31.4	102.5
50	24.1	125.3			
60	28.7	123.6			

Bold numbers indicate local minima.

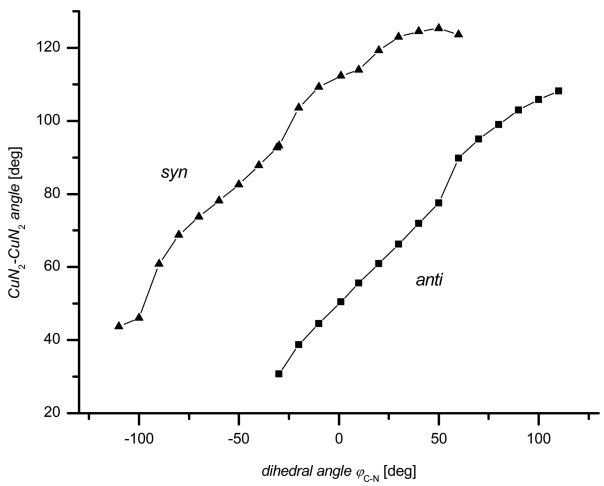

Figure 12. Changes in CuN_2—CuN_2 dihedral angle dependent on rotation along the C—$N_{imine,gua}$ single bond.

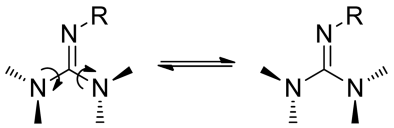

Scheme 3. Orientations of the NMe_2 groups in the guanidine moiety.

hindered. In aliphatic free ligands, this rotation is frozen at room temperature whereas in aromatic guanidines it can be observed by means of NMR spectroscopy.[10] Whether the coordination of copper shows any influence is unknown.

TD-DFT calculations using B3LYP/def2-TZVP of selected twisted structures optimized with BP86/6-311G(d) have been performed. The PES was analyzed for angles $\angle(CuN_2—CuN_2)$ between 20 and 120° with the minimum at about 70°. The spectra are shown in Figures 13 and 14 for more clarity. The band shifts have been indicated with arrows going from smaller to larger torsion angles. The first small band at 2 eV shifts on both sides of the potential curve to smaller energies, decreases in intensity and disappears at 20°. The second band at 2.5 eV and the third one at 3.5 eV are separated at 70°, both converge on both sides of the potential curve until they completely merge at 20°. At angles of >70°, the third band splits and a further band appears which almost converges with the large UV band (120°, ~4.5 eV). On the left side of the potential curve between 20 and 70°, the large UV band gains a shoulder (20°, 4 eV) whereas the UV band itself shifts only slightly for small angles to small energies and for larger angles to larger energies. Remarkably, the strong intensity decrease is observable in both sides of the potential curve. In summary, the relative and absolute positions of the calculated bands are strongly dependent on the degree of distortion in the molecule.

TD-DFT and MBPT studies on a small model system

In order to probe the applicability of TD-DFT for the system considered here and in order to provide meaningful error bars,

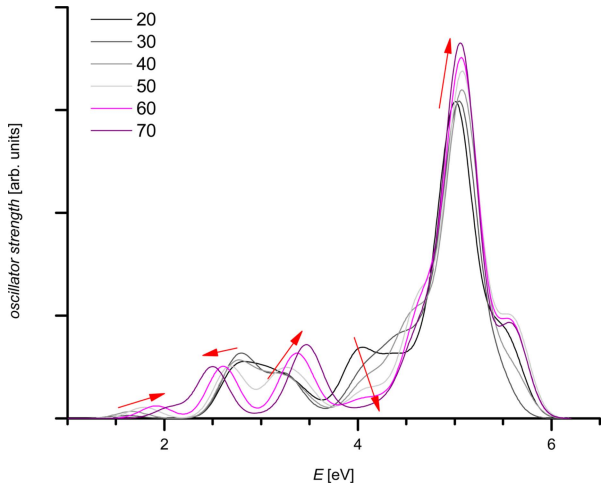

Figure 13. TD calculations combined with a PES analysis of the angle $\angle(CuN_2—CuN_2)$ between 20 and 70°. The band shifts have been indicated with arrows going from smaller to larger torsion angles. [Color figure can be viewed in the online issue, which is available at wileyonlinelibrary.com.]

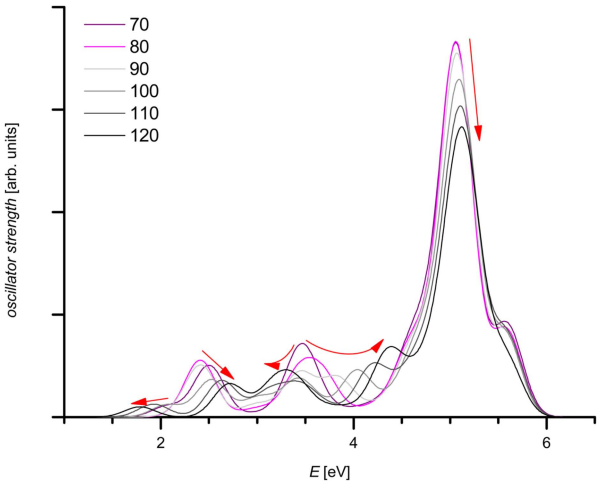

Figure 14. TD calculations combined with a PES analysis of the angle $\angle(CuN_2—CuN_2)$ between 70 and 120°. The band shifts have been indicated with arrows going from smaller to larger torsion angles. [Color figure can be viewed in the online issue, which is available at wileyonlinelibrary.com.]

we perform additional benchmark calculations for a small model system which contains the three hallmarks of the large $[Cu(TMGqu)_2]^+$ system: it is a bis(chelate) copper(I) complex with two different donors being a guanidine and an imine function (Scheme 4). The calculations have been done with def2-TZVP or using plane waves (pw).

For both Cu(I) complexes general differences in the structural parameters for the various functionals are to be mentioned. Thus, for the large $[Cu(TMGqu)_2]^+$ system the Cu—N bonds are predicted about 0.06 Å longer with B3LYP than with PW91. The C=N bond of the guanidine is about 0.01 Å shorter with B3LYP, the C—N bonds show no significant difference. Comparable trends are found for the small system with Cu(I). Additionally, the small system shows 0.041 (0.029) Å (here and further in parentheses: PW91) shorter Cu-N_{gua} bonds, while the Cu—N bonds to the second imine donor are 0.028 (0.026) Å longer as compared to the quinoline. The C—N bonds are about 0.008–0.014 (0.009–0.014) Å shorter for the small system. The chelate angle between the coordination planes increases from 78 (75)° to almost 90°. For the small system no changes are seen for the Cu—$N_{imine,gua}$ bond with B3LYP, the second Cu—N bond length increases about 0.02 Å. The C—N bond lengths in the guanidine decrease about 0.01 Å. The chelate angle shows no significant change. Table 7 shows furthermore that the influence of the basis set is small compared to the impact of the XC functional: the structural parameters obtained using the complete and orthogonal pw basis set are close to the ones derived from localized-orbital calculations using the same XC functional.

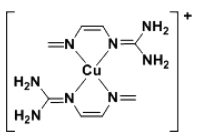

Scheme 4. Small model system for comparative DFT and GW studies.

Table 7. Selected bond lengths (Å) and angles (°) for calculated structures of the $[Cu(TMGqu)_2]^+$ cation and the small model system at various levels of theory.

Cu(I)	Method	Cu—$N_{imine,gua}$ (Å)	Cu—N_{imine} (Å)	C=$N_{imine,gua}$ (Å)	C—N_{amine} (Å)		CuN_2—CuN_2 (°)
small	B3LYP/def2-TZVP	2.133	2.080	1.312	1.354	1.357	87.3
small	PW91/def2-TZVP	2.083	2.022	1.323	1.356	1.360	87.4
small	PW91/pw	2.073	1.977	1.325	1.358	1.360	86.5
large	B3LYP/def2-TZVP	2.174	2.052	1.320	1.362	1.371	77.8
large	PW91/def2-TZVP	2.112	1.996	1.332	1.366	1.374	74.6
large	PW91/pw	2.103	1.974	1.335	1.367	1.355	73.5

For TD calculations, it was already seen from the benchmarking results that differences in the structural parameters have less influence on the transition positions than the choice of functional. In Figure 15, it is depicted that with PW91 not only a shift of the bands to smaller energies but also differences in the structure and relative positions of the bands (as compared to B3LYP) are found.

With an even higher amount of Hartree-Fock exchange (BHLYP), the calculated spectrum changes drastically. If for the pure GGA BLYP (compare Fig. 16) three bands are found, with the second one showing the largest intensity, than with addition of 20% HF exchange (B3LYP) the bands are only shifted to higher energies and the distance between the first two bands decreases. With BHLYP, the first band is the most intensive, and appears at higher energies (4.7eV) than the first two bands with BLYP and B3LYP (3.8 and 4.3eV). The other bands are much less intensive and are shifted far into the UV range. The Coulomb-attenuating CAM-B3LYP also yields blue-shifted band positions, but the spectrum structure is comparable to the B3LYP calculation. The distance between the smaller first band and the intensive second decreases even further, and an additional shoulder to the second band appears. Another two less intensive bands are predicted at higher energies. Hence, the influence of the functional on the spectrum and the position of the bands are very dramatic.

To comprehend the impact of the differences between the large and the small system on the TD results, the molecular orbitals are compared. For the large $[Cu(TMGqu)_2]^+$ system, seven of the occupied and six of the unoccupied frontier orbitals are plotted for both functionals (Fig. 17), with $E = 0$ lying at half distance of the HOMO–LUMO gap. The occupied orbitals are of Cu-d character and show considerable similarities for both functionals. HOMO and HOMO−1 with B3LYP are almost identical as with PW91, the other orbitals show divergence in order and form. Thus, HOMO−6 (B3LYP) corresponds to HOMO−4 (PW91) and the ligand involvement observed in HOMO−2 and HOMO−3 (B3LYP) is seen for HOMO−5 and HOMO−6 with PW91. The HOMO has antibonding character in respect to all N donor functions, HOMO−1 to HOMO−4 all show bonding overlapping with the N donor functions.

The relative energy differences of the occupied orbitals are very similar. The HOMO–LUMO gap for B3LYP is larger than for PW91, which leads to the already discussed shift of the first Vis band to larger energies. The six unoccupied orbitals shown in Figure 17 are all of π^* ligand character, every two being linear combinations of π^* orbitals of the quinoline and the guanidine, and to some extent, degenerate. For both functionals, the form and relative energies of examined LUMOs are the same, apart from slight differences in order of the almost degenerated orbital pairs. Because the dominant bands in Vis

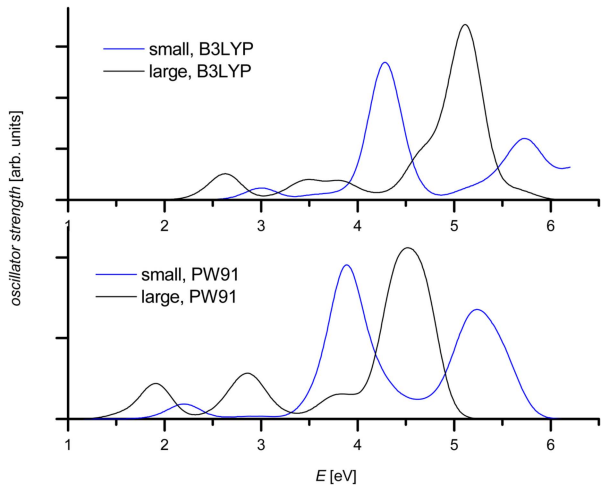

Figure 15. TD spectra of the $[Cu(TMGqu)_2]^+$ cation and the small model system at B3LYP and PW91 levels of theory. [Color figure can be viewed in the online issue, which is available at wileyonlinelibrary.com.]

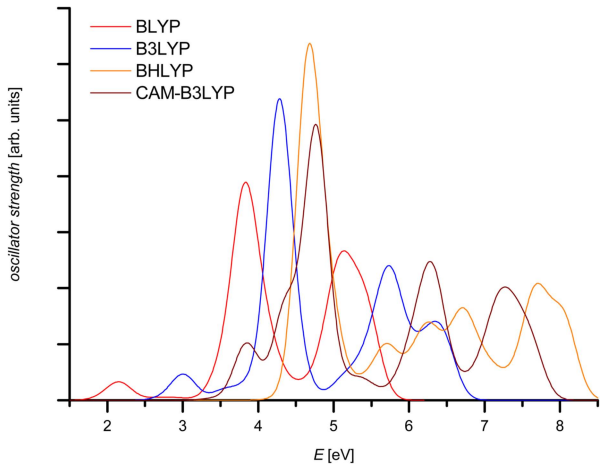

Figure 16. TD spectra of the small model system at various levels of theory showing the influence of the amount of exact HF exchange. [Color figure can be viewed in the online issue, which is available at wileyonlinelibrary.com.]

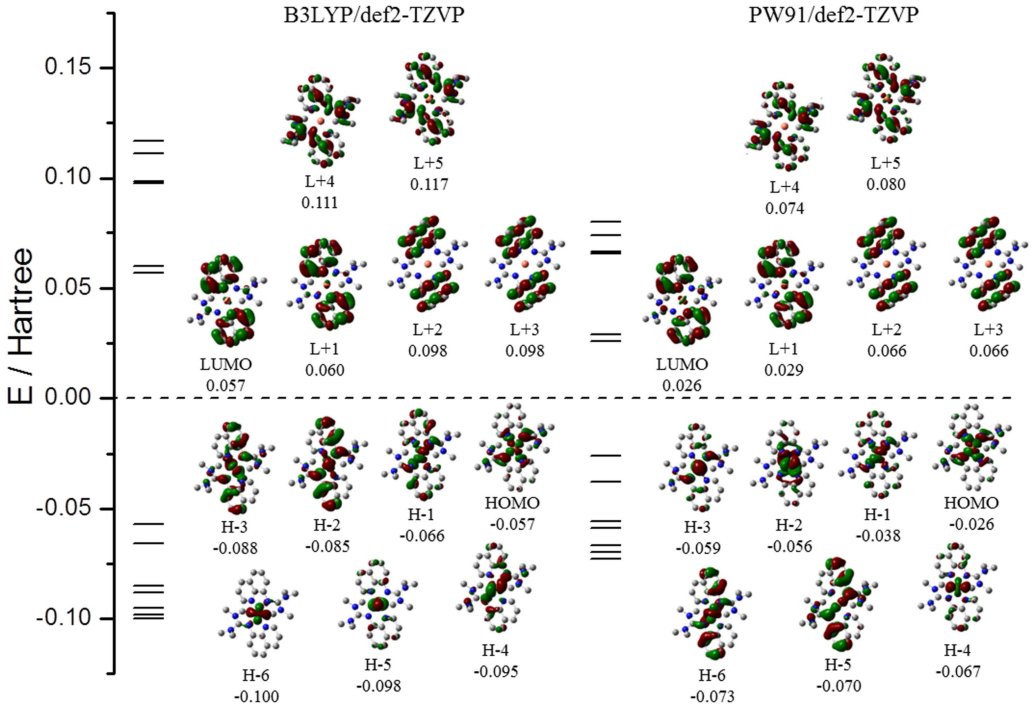

Figure 17. Molecular orbitals of the $[Cu(TMGqu)_2]^+$ cation at B3LYP/def2-TZVP and PW91/def2-TZVP levels of theory. [Color figure can be viewed in the online issue, which is available at wileyonlinelibrary.com.]

range stem from HOMO/HOMO−1 to LUMO/LUMO+1 transitions and also for UV bands transitions either from or to frontier orbitals are found, the nature of the Vis bands and to some extent UV bands can be predicted equally well with both functionals.

In Figure 18, nine occupied and six unoccupied orbitals of the small system are plotted. HOMO−7 and HOMO−8 are of occupied π^* guanidine character for both functionals. HOMO–HOMO−6 are Cu-d orbitals with even more mixing of ligand orbitals. HOMO and HOMO−1 are again equal for both functionals, the ligand involvement with PW91 is more pronounced for lower-lying orbitals. The absence of the quinoline ring in the small system leads to higher energy LUMOs and thus to a larger HOMO–LUMO gap. The LUMOs for both functionals are

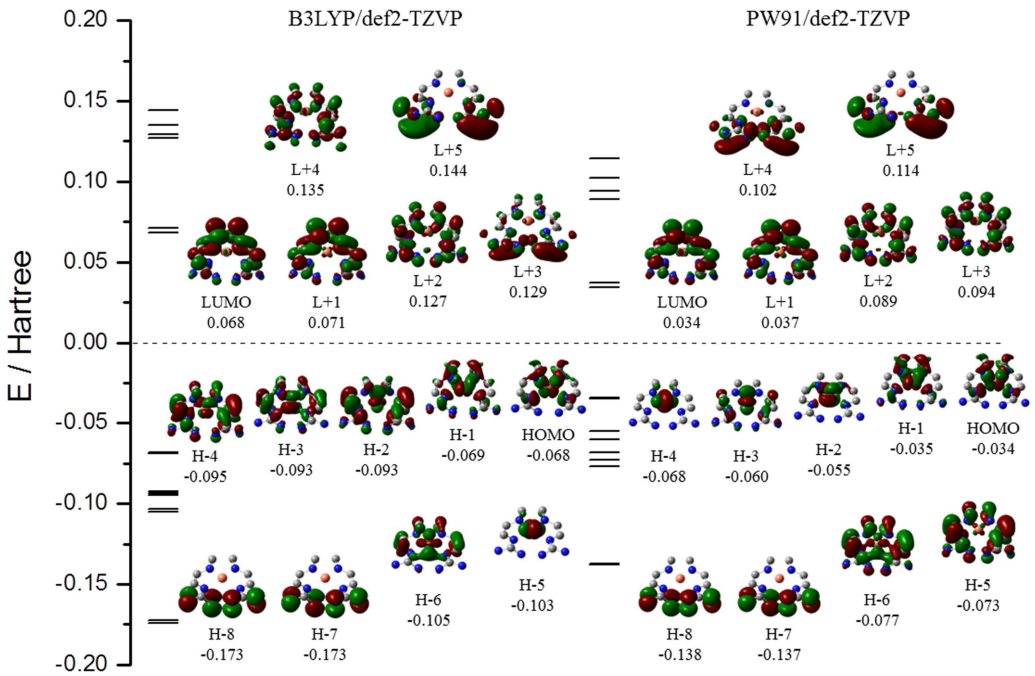

Figure 18. Molecular orbitals of the small model system at B3LYP/def2-TZVP and PW91/def2-TZVP levels of theory. [Color figure can be viewed in the online issue, which is available at wileyonlinelibrary.com.]

of unoccupied π^* ligand character, showing again some extent of degeneracy. A larger difference can be noted for B3LYP, where LUMO+3, with electron density on the guanidines, and LUMO+4, a mixed guanidine–imine orbital, have changed places. Overall, the great similarity of the frontier orbitals for both functionals yields structurally similar TD spectra, which even though differ in positions of the bands due to higher HOMO–LUMO gap with B3LYP.

The theoretical absorption bands of the small system (Fig. 15) can all be assigned to MLCT transitions. Thus, for B3LYP (in parentheses: PW91) the small band at 3.0 eV (2.3 eV) stems from transitions from HOMO and HOMO−1 Cu-d orbitals to the lowest π^* ligand orbitals of LUMO and LUMO+1. The big band at 4.3 eV (3.9 eV) derives from transitions from lower Cu-d orbitals to LUMO and LUMO+1, whereas the band at 5.8 eV (5.3 eV) stems from transitions from HOMO and HOMO−1 to higher π^* orbitals of the ligands.

In Figure 19, we compare the molecular eigenvalue spectrum calculated using local orbitals as well as plane waves. On the DFT level of theory, good agreement is found for the occupied states that agree with respect to the relative order and absolute energy within about a few tenths of one eV. This is in accordance with our previous finding that the structural description obtained with either the def2-TZVP or the pw do largely agree. Naturally, localized basis functions are less well suited to describe energetically higher excited states. Therefore, the deviations between the def2-TZVP and the pw results increase with increasing energy. In particular, the calculated band gap is larger when local orbitals are used to expand the wave functions.

The quasiparticle spectra obtained with the GWA using a plane-wave basis are also shown in Figure 19. Single-shot G_0W_0 calculations open the gap from about 1.77 eV within DFT-PW91 to 5.74 eV. Calculations within B3LYP start already from a larger band gap of 3.43 eV using plane waves, which is further opened to 6.68 eV in G_0W_0. We also studied the influence of self-consistency on the quasiparticle energies by updating the Green's function G.[76] It is found that two updates of G lead to nearly converged quasiparticle energies that feature now an even larger HOMO–LUMO gap of 6.63 eV (PW91) and 7.05 eV (B3LYP). Obviously the band gap obtained starting from the local XC functional is more affected by self-consistency effects than the B3LYP results. This indicates that the latter provides a better approximation to the actual electronic structure than obtained within the local XC functional. In any event, our calculations yield large electron self-energy effects of the order of several electronvolts. In particular, the energy order of the molecular states is influenced by the self-energy corrections.

In Figure 20, optical spectra obtained within different levels of theory are compared to TD-DFT results. Interestingly, already the calculations on the IPA level describe the optical response qualitatively correctly, in particular in case of the B3LYP functional. The absolute peak positions, however, deviate from the TD-DFT results. In case of PW91 calculations, the IPA results consistently underestimate the TD-DFT excitation energies by up to nearly 1 eV. The energy deviations are

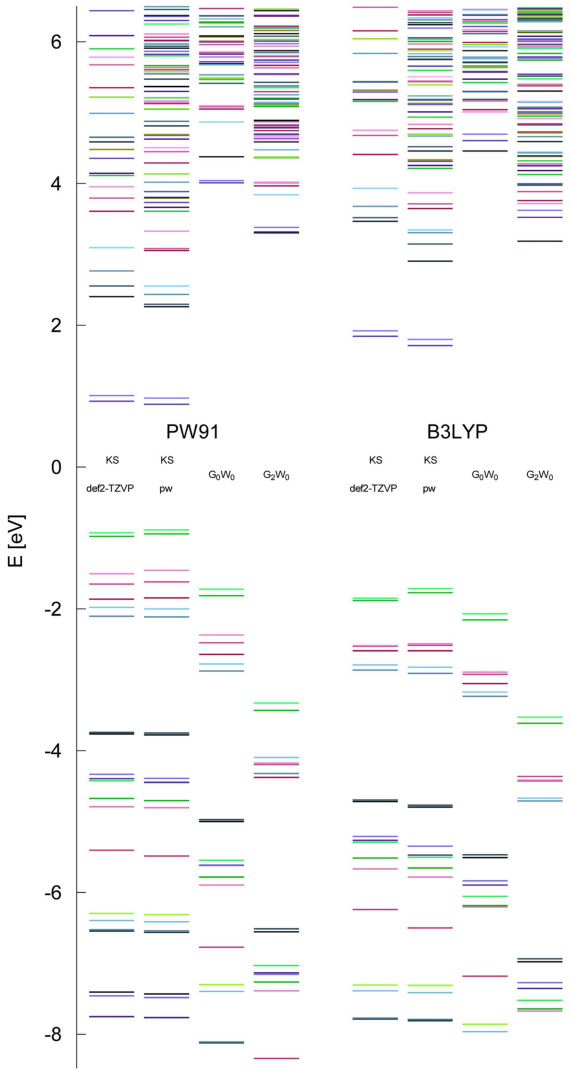

Figure 19. Molecular orbital spectra of $[CuN_8C_8H_{16}]^+$. Colour marking is only strictly consistent within the same functional for plane wave and GW calculations. [Color figure can be viewed in the online issue, which is available at wileyonlinelibrary.com.]

smaller, and of opposite sign, in case of the B3LYP results. In any event, the present results suggest that the single-particle DFT orbitals for the system investigated here allow for a meaningful qualitative interpretation of the excited-state properties. The first feature in the PW91 IPA spectrum at 1.9 eV, for example, consists of four single particle transitions. In TD-DFT, this feature appears at 2.2 eV, consisting of two mixed transitions that involve the same orbitals, namely HOMO−1, HOMO, LUMO, and LUMO+1. The inclusion of many-body effects via GW+BSE calculations leads to an even better agreement with the TD-DFT results. This holds in particular for the PW91 results, where the TD-DFT and GW+BSE spectra largely agree. Thereby we note a strong influence of the TDA on the calculated optical response. It blue-shifts the absorption energies and also substantially modifies the line shape as compared to the solution of the BSE where also the resonant–nonresonant coupling terms were taken into account. The results from the full BSE agree closely with the TD-DFT results, in particular

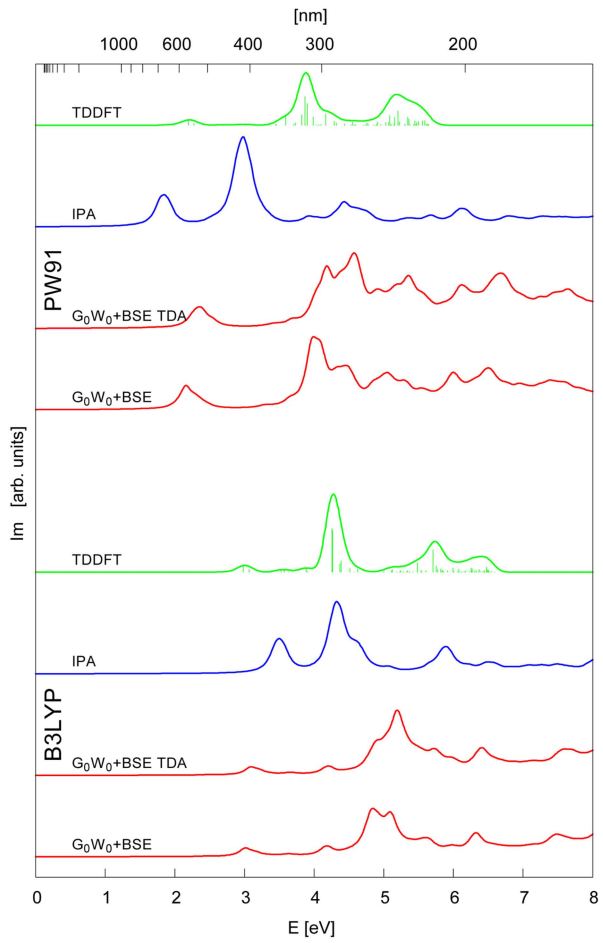

Figure 20. Optical spectra of $[CuN_8C_8H_{16}]^+$ calculated within different levels of theory, that is, TD-DFT, IPA, and from MBPT (GW+BSE). The calculations are based either on the PW91 or the B3LYP XC functional. [Color figure can be viewed in the online issue, which is available at wileyonlinelibrary.com.]

concerning the energy positions of the low-energy excitations. Altogether, however, the system investigated is, at least concerning its low-energy excitations, remarkably robust with respect to both the physical approximations as well as the numerical details of the calculations. A meaningful description of its electronic structure is already possible within DFT, using the B3LYP XC functional. Essentially, the changes observed upon calculating the optical response either within the TD-DFT or by using MBPT Green's function methods are of the same order of magnitude as expected from the usage of different basis sets.

Conclusions

In summary, we could show that the correct description of bis(chelate) copper complexes requires extensive benchmarking. The geometric benchmarking recommends the BP86/6-311G(d) methodology for best accordance of gas-phase calculations to the solid state structures from X-ray measurements whereas the optical benchmarking gives best resemblance to experimental spectra when applying the combination B3LYP/def2-TZVP. With the large real-life copper complex, we have thoroughly studied the spectral sensitivity on torsion of copper coordination, isomer formation as well as choice of functionals and basis sets. Here, we found a very strong influence of the angle between the chelate planes. The correct description of the copper coordination is crucial for the prediction of optical spectra. In order to assess the methodological influence on the calculated ground- and excited-state properties, we performed in addition to (TD-)DFT also MBPT calculations, considering a small model system. It is found that large quasiparticle energies of the order of several electronvolts are largely offset by exciton binding energies for optical excitations. For this reason, optical-response calculations on the IPA level of theory are in qualitative (and in case of the B3LYP functional near quantitative) agreement with the TD-DFT results. From the comparison between TD-DFT and MBPT, we conclude that at least the low-energy excitations are remarkably robust with respect to the approximations made in their description. While MBPT methods are for computational reasons not yet applicable to large bis(chelate) copper complexes, the present results indicate that their excitations can be meaningfully modelled within TD-DFT. Hence, provided a careful benchmarking is performed, CT excitations in copper complexes are accessible to a quantitative analysis based on DFT.

Acknowledgments

Generous grants of computer time at the Höchstleistungs-Rechenzentrum Stuttgart and the Paderborn Center for Parallel Computing PC^2 are gratefully acknowledged.

Keywords: copper complex • charge transfer • TD-DFT • MBPT • GW

How to cite this article: A. Jesser, M. Rohrmüller, W. G. Schmidt, S. Herres-Pawlis. *J. Comput. Chem.* **2014**, *35*, 1–17. DOI: 10.1002/jcc.23449

[1] A. Lavie-Cambot, M. Cantuel, Y. Leydet, G. Jonusauskas, D. M. Bassani, N. D. McClenaghan, *Coord. Chem. Rev.* **2008**, *252*, 2572.
[2] L. M. Mirica, X. Ottenwaelder, T. D. P. Stack, *Chem. Rev.* **2004**, *104*, 1013.
[3] D. B. Rorabacher, *Chem. Rev.* **2004**, *104*, 651.
[4] K. A. Jorgensen, T. B. Poulsen, *Chem. Rev.* **2008**, *108*, 2903.
[5] E. Ruiz, C. de Graaf, P. Alemany, S. Alvarez, *J. Phys. Chem. A* **2002**, *106*, 4938.
[6] M. G. Fraser, H. van der Salm, S. A. Cameron, A. G. Blackman, K. C. Gordon, *Inorg. Chem.* **2013**, *6*, 2980.
[7] K. D. Karlin, S. Itoh, S. Rokita, Eds. Copper-Oxygen Chemistry: Wiley Series of Reactive Intermediates 4; Wiley: Hoboken, New Jersey, **2011**.
[8] B. Meunier, Ed. Metal-Oxo and Metal-Peroxo Species in Catalytic Oxidations, Structure and Bonding 97; Springer: Berlin and Heidelberg, **2000**.
[9] P. Comba, M. Kerscher, *Coord. Chem. Rev.* **2009**, *253*, 564.
[10] S. Herres-Pawlis, A. Neuba, O. Seewald, T. Seshadri, H. Egold, U. Flörke, G. Henkel, *Eur. J. Org. Chem.* **2005**, 4879.
[11] M. Tamm, D. Petrovic, S. Randoll, S. Beer, T. Bannenberg, P. G. Jones, J. Grunenberg, *Org. Biomol. Chem.* **2007**, *5*, 523.
[12] P. Roquette, C. König, O. Hübner, A. Wagner, E. Kaifer, M. Enders, H.-J. Himmel, *Eur. J. Inorg. Chem.* **2010**, 4770.
[13] S. Herres-Pawlis, U. Flörke, G. Henkel, *Eur. J. Inorg. Chem.* **2005**, 3815.

[14] R. Haase, T. Beschnitt, U. Flörke, S. Herres-Pawlis, *Inorg. Chim. Acta* **2011**, *374*, 546.
[15] O. Bienemann, R. Haase, A. Jesser, T. Beschnitt, A. Döring, D. Kuckling, I. dos Santos Vieira, U. Flörke, S. Herres-Pawlis, *Eur. J. Inorg. Chem.* **2011**, *15*, 2367.
[16] O. Bienemann, R. Haase, U. Flörke, A. Döring, D. Kuckling, S. Herres-Pawlis, *Z. Naturforsch. B* **2010**, *65b*, 798.
[17] F. Neese, *J. Biol. Inorg. Chem.* **2006**, *11*, 702.
[18] R. Haase, Sauerstoffaktivierung und –übertragung durch Kupfer-Komplexe mit polyfunktionellen Guanidinliganden, Dissertation, Universität Paderborn, Paderborn, Germany, **2011**.
[19] P. R. Varadwaj, H. M. Marques, *Theor. Chem. Acc.* **2010**, *127*, 711.
[20] D. Mikulski, M. Molski, *J. Mol. Struct. THEOCHEM.* **2010**, *956*, 66.
[21] A. Kovalevsky, M. Gembicky, I. Novozhilova, P. Coppens, *Inorg. Chem.* **2003**, *42*, 8794.
[22] Z. A. Siddique, Y. Yamamoto, T. Ohno, K. Nozaki, *Inorg. Chem.* **2003**, *42*, 6366.
[23] C. A. Ullrich, Time-Dependent Density-Functional Theory: Concepts and Applications; Oxford University Press: Oxford, **2012**.
[24] G. Onida, L. Reining, A. Rubio, *Rev. Mod. Phys.* **2002**, *74*, 601.
[25] M. J. Frisch, G. W. Trucks, H. B. Schlegel, G. E. Scuseria, M. A. Robb, J. R. Cheeseman, G. Scalmani, V. Barone, B. Mennucci, G. A. Petersson, H. Nakatsuji, M. Caricato, X. Li, H. P. Hratchian, A. F. Izmaylov, J. Bloino, G. Zheng, J. L. Sonnenberg, M. Hada, M. Ehara, K. Toyota, R. Fukuda, J. Hasegawa, M. Ishida, T. Nakajima, Y. Honda, O. Kitao, H. Nakai, T. Vreven, J. A. Montgomery, Jr., J. E. Peralta, F. Ogliaro, M. Bearpark, J. J. Heyd, E. Brothers, K. N. Kudin, V. N. Staroverov, T. Keith, R. Kobayashi, J. Normand, K. Raghavachari, A. Rendell, J. C. Burant, S. S. Iyengar, J. Tomasi, M. Cossi, N. Rega, J. M. Millam, M. Klene, J. E. Knox, J. B. Cross, V. Bakken, C. Adamo, J. Jaramillo, R. Gomperts, R. E. Stratmann, O. Yazyev, A. J. Austin, R. Cammi, C. Pomelli, J. W. Ochterski, R. L. Martin, K. Morokuma, V. G. Zakrzewski, G. A. Voth, P. Salvador, J. J. Dannenberg, S. Dapprich, A. D. Daniels, O. Farkas, J. B. Foresman, J. V. Ortiz, J. Cioslowski, D. J. Fox, Gaussian 09, Revision B.01; Gaussian, Inc.: Wallingford CT, **2010**.
[26] J. P. Perdew, *Phys. Rev. B* **1986**, *33*, 8822.
[27] A. D. Becke, *Phys. Rev. A* **1988**, *38*, 3098.
[28] C. Lee, W. Yang, R. G. Parr, *Phys. Rev. B* **1988**, *37*, 785.
[29] B. Miehlich, A. Savin, H. Stoll, H. Preuss, *Chem. Phys. Lett.* **1989**, *157*, 200.
[30] J. P. Perdew, J. A. Chevary, S. H. Vosko, K. A. Jackson, M. R. Pederson, D. J. Singh, C. Fiolhais, *Phys. Rev. B* **1992**, *46*, 6671.
[31] J. P. Perdew, K. Burke, Y. Wang, *Phys. Rev. B* **1996**, *54*, 16533.
[32] K. Burke, J. P. Perdew, Y. Wang, In Electronic Density Functional Theory: Recent Progress and New Directions; J. F. Dobson, G. Vignale, M. P. Das, Eds.; Plenum: New York, **1998**.
[33] A. D. Becke, *J. Chem. Phys.* **1993**, *98*, 5648.
[34] P. J. Stephens, F. J. Devlin, C. F. Chabalowski, M. J. Frisch, *J. Phys. Chem.* **1994**, *98*, 11623.
[35] C. Adamo, V. Barone, *J. Chem. Phys.* **1999**, *110*, 6158.
[36] J. M. Tao, J. P. Perdew, V. N. Staroverov, G. E. Scuseria, *Phys. Rev. Lett.* **2003**, *91*, 146401.
[37] J.-D. Chai, M. Head-Gordon, *Phys. Chem. Chem. Phys.* **2008**, *10*, 6615.
[38] T. Yanai, D. Tew, N. Handy, *Chem. Phys. Lett.* **2004**, *393*, 51.
[39] W. J. Hehre, R. Ditchfield, J. A. Pople, *J. Chem. Phys.* **1972**, *56*, 2257.
[40] P. C. Hariharan, J. A. Pople, *Theor. Chim. Acta* **1973**, *28*, 213.
[41] V. A. Rassolov, J. A. Pople, M. A. Ratner, T. L. Windus, *J. Chem. Phys.* **1998**, *109*, 1223.
[42] A. J. H. Wachters, *J. Chem. Phys.* **1970**, *52*, 1033.
[43] P. J. Hay, *J. Chem. Phys.* **1977**, *66*, 4377.
[44] K. Raghavachari, G. W. Trucks, *J. Chem. Phys.* **1989**, *91*, 1062.
[45] T. Clark, J. Chandrasekhar, G. W. Spitznagel, P. V. R. Schleyer, *J. Comput. Chem.* **1983**, *4*, 294.
[46] M. J. Frisch, J. A. Pople, J. S. Binkley, *J. Chem. Phys.* **1984**, *80*, 3265.
[47] F. Weigend, R. Ahlrichs, *Phys. Chem. Chem. Phys.* **2005**, *7*, 3297.
[48] S. I. Gorelsky, SWizard program; University of Ottawa: Ottawa, Canada, **2013**. Available at: http://www.sg-chem.net/, accessed on 17.04.2013.
[49] S. I. Gorelsky, A. B. P. Lever, *J. Organomet. Chem.* **2001**, *635*, 187.
[50] G. Kresse, J. Furthmüller, *Comput. Mater. Sci.* **1996**, *6*, 15.
[51] P. E. Blöchl, *Phys. Rev. B* **1994**, *50*, 17953.
[52] H. Ehrenreich, M. H. Cohen, *Phys. Rev.* **1959**, *115*, 786.
[53] S. L. Adler, *Phys. Rev.* **1962**, *126*, 413.
[54] N. Wiser, *Phys. Rev.* **1963**, *129*, 62.
[55] M. Gajdos, K. Hummer, G. Kresse, J. Furthmüller, F. Bechstedt, *Phys. Rev. B* **2006**, *73*, 045112.
[56] V. Olevano, L. Reining, *Phys. Rev. Lett.* **2001**, *86*, 5962.
[57] L. Hedin, *Phys. Rev.* **1965**, *139*, A796.
[58] F. Bechstedt, In Festkörperprobleme: Advances in Solid State Physics, Vol. *32*; U. Rössler, Ed.; Vieweg: Braunschweig/Wiesbaden, **1992**; p. 161.
[59] M. Shishkin, G. Kresse, *Phys. Rev. B* **2006**, *74*, 035101.
[60] F. Bechstedt, R. Del Sole, G. Cappellini, L. Reining, *Solid State Commun.* **1992**, *84*, 765.
[61] A. Hermann, W. G. Schmidt, P. Schwerdtfeger, *Phys. Rev. Lett.* **2008**, *100*, 207403.
[62] P. H. Hahn, W. G. Schmidt, K. Seino, M. Preuss, F. Bechstedt, J. Bernholc, *Phys. Rev. Lett.* **2005**, *94*, 037404.
[63] A. Riefer, E. Rauls, W. G. Schmidt, J. Eberhard, I. Stoll, J. Mattay, *Phys. Rev. B* **2012**, *85*, 165202.
[64] M. Rohrmüller, S. Herres-Pawlis, M. Witte, W. G. Schmidt, *J. Comput. Chem.* **2013**, *34*, 1035.
[65] Y. Ma, M. Rohlfing, C. Molteni, *Phys. Rev. B* **2009**, *80*, 241405.
[66] C. Ambrosch-Draxl, D. Nabok, P. Puschnig, C. Meisenbichler, *New J. Phys.* **2009**, *11*, 125010.
[67] M. Grüning, A. Marini, X. Gonze, *Nano Lett.* **2009**, *9*, 2820.
[68] J. M. Garcia-Lastra, K. S. Thygesen, *Phys. Rev. Lett.* **2011**, *106*, 187402.
[69] W. G. Schmidt, S. Glutsch, P. H. Hahn, F. Bechstedt, *Phys. Rev. B* **2003**, *67*, 085307.
[70] L. Yang, D. R. Powell, R. P. Houser, *Dalton Trans.* **2007**, 955.
[71] V. Raab, K. Harms, J. Sundermeyer, B. Kovacevic, Z. Maksic, *J. Org. Chem.* **2003**, *68*, 8790.
[72] S. Grimme, *J. Comput. Chem.* **2006**, *27*, 1787.
[73] K. Born, P. Comba, M. Kerscher, G. Linti, H. Pritzkow, H. Rohwer, *Dalton Trans.* **2009**, 362.
[74] R. L. Martin, *J. Chem. Phys.* **2003**, *118*, 4775.
[75] I. dos Santos Vieira, Zinkkomplexe mit neutralen N-Donorliganden als Katalysatoren der Ringöffnungspolymerisation von Lactid, Dissertation, Technische Universität Dortmund, Dortmund, Germany, **2013**.
[76] M. Shishkin, G. Kresse, *Phys. Rev. B* **2007**, *75*, 235102.

Received: 17 May 2013
Revised: 19 August 2013
Accepted: 21 August 2013
Published online on 2 October 2013